World Electric Vehicle Journal

MDPI

Article

Two-Stage Optimal Scheduling for Virtual Power Plants Considering Scheduling Success Probability of Multi-Agent Demand-Side Resources

Yukun Jin [1], Xiaopeng Li [1], Siyuan Cai [1], Yipin Han [1], Shuo Gao [2], Minghao Du [2] and Donglai Wang [2,*]

[1] State Grid Anshan Electric Power Supply Company, State Grid Liaoning Electric Power Supply Co., Ltd., Anshan 114000, China
[2] Key Laboratory of Regional Multi-Energy System Integration and Control of Liaoning Province, Shenyang Institute of Engineering, Shenyang 110136, China
* Correspondence: wangdl@sie.edu.cn

Abstract

High penetration of renewable energy imposes greater demands on the scheduling flexibility of demand-side resources in virtual power plant (VPP) dispatch. Nevertheless, heterogeneous resources exhibit remarkable differences in response reliability, and electric vehicles (EVs) in particular show distinct execution performance between orderly charging and vehicle-to-grid (V2G) modes. To tackle this issue, this paper proposes a two-stage optimal scheduling strategy for multi-agent VPPs incorporating scheduling success probability. A quantitative model for the effective dispatch contribution coefficient is constructed from two dimensions, i.e., relative capacity weight and dispatch execution reliability, with differentiated parameters tailored for EV charging and V2G modes. The two-stage leader–follower game problem is decoupled via backward induction, and the optimal dispatch price is rigorously derived through Karush–Kuhn–Tucker conditions. A 24 h case study covering wind power, photovoltaics, energy storage, EVs, and air-conditioning loads validates the proposed method. Results indicate that the strategy boosts total VPP revenue by 7.43% compared with independent operation, lifts the renewable energy accommodation rate from 88.3% to 94.6%, and reduces the average operating cost by 19 CNY/MWh. Through dual-mode differentiated scheduling, EVs achieve 5.10% revenue growth and serve as a key flexible resource for VPP economic operation.

Keywords: VPP; generalized demand-side resources; scheduling success probability; two-stage optimization; electric vehicles; V2G

Academic Editor: Michael Fowler

Received: 7 August 2026
Revised: 10 September 2026
Accepted: 11 September 2026
Published: 15 September 2026

1. Introduction

Substantial uncertainty and volatility have been introduced into modern power system operations by the rapidly growing penetration of renewable energy resources [1]. Although flexible thermal generating units remain responsible for critical power regulation services, their inherent regulation capability is becoming increasingly inadequate to accommodate high shares of renewable generation. Accordingly, full utilization of the regulation potential embedded in distributed demand-side resources is required to deliver supplementary ancillary services to the power system [2]. Meanwhile, a transition toward high-efficiency, low-carbon, and sustainable development is underway in modern power systems [3]. As supply-side regulation resources approach their practical physical limits, demand-side flexible resources have emerged as a pivotal source of system scheduling flexibility [4]. Typical adjustable demand-side resources encompass distributed photovoltaic units, distributed wind turbines, controllable air-conditioning loads, electric vehicles, and battery energy storage systems. These resources are generally characterized by low individual rated capacity and geographic dispersion [5], which makes direct participation in bulk power system dispatch infeasible for individual resources. Coordinated control of electricity–hydrogen DC microgrids [6] and capacity planning and optimal dispatch of second-life battery energy storage systems [7] have been investigated in existing literature, corroborating the techno-economic value of collaborative resource aggregation. Nevertheless, the aggregation and scheduling mechanisms for heterogeneous demand-side resources remain insufficiently explored.

In this context, virtual power plants (VPPs) have been established as an effective technical framework for the aggregated management of multi-agent generalized demand-side resources [8]. Extensive research has been conducted on VPP optimal scheduling and microgrid energy management, including dual-ANN-based optimization for efficient microgrid energy management [9] and design and performance evaluation of islanded hybrid microgrids [10]. Reference [11] developed a probabilistic scheduling model for VPPs integrating energy storage systems and demand response programs. In [12], interval optimization was combined with deterministic optimization to address the stochastic uncertainty associated with VPP demand response. Optimal bidding strategies for VPPs with hybrid resource portfolios have also been systematically examined [13].

For benefit allocation under quasi-linear demand response, a grid–load cooperative game mechanism based on Nash bargaining theory has been proposed in prior work [14]. A multi-leader, multi-follower bi-level game model was formulated in [15], where the system operator serves as the leader and load aggregators, energy storage stations, and wind farm operators act as followers. Coordinated operation strategies for integrated energy service providers and multi-stakeholder user communities were explored in [16] via a nonlinear multi-objective optimization framework. Furthermore, VPP demand response trading models that account for consumer satisfaction and expected response volume have been developed [17]. A stochastic mixed-integer linear programming model incorporating distribution network operational constraints was formulated in [18]. A VPP revenue allocation scheme based on the Nash–Harsanyi bargaining solution was proposed in [19], while VPP coordinated dispatch strategies under extreme distribution network scenarios were analyzed in [20]. Overall, most existing studies have focused primarily on revenue allocation and risk control for VPPs operating in multi-market environments [21].

With the deepening integration of source–grid–load–storage resources and rising renewable energy penetration, optimal VPP scheduling has attracted extensive research attention. VPP scheduling can be broadly classified into internal scheduling and external scheduling according to the dispatch boundary. In internal scheduling, generation and load response plans are allocated among internal entities by the VPP dispatch center, with the core objective of maximizing the overall economic benefits of the VPP.

Fuzzy optimization theory was introduced in [22] to construct a two-stage scheduling model for VPPs comprising renewable energy units, conventional generators, and demand response resources. In [23], thermal units, wind farms, photovoltaic stations, carbon capture devices, and electric boilers were incorporated into the scheduling framework, and a VPP scheduling model with demand response was established to improve economic efficiency and reduce carbon emissions. Wind power, photovoltaics, absorption chillers, and carbon trading mechanisms were integrated into the optimal scheduling system in [24]. A two-stage dynamic robust optimization model accounting for carbon trading and multi-dimensional source-load uncertainties was developed in [25]. In [26], wind turbines,

https://doi.org/10.3390/wevj17090484

photovoltaic units, gas turbines, energy storage systems, and controllable flexible loads were aggregated, and compressed air energy storage was introduced to enhance the overall regulation capability of VPPs. Collectively, these studies demonstrate the economic value of internal resource coordination within VPPs.

Unlike internal scheduling, external scheduling focuses on VPP participation in centralized power system dispatch and is typically coupled with internal scheduling models to form a canonical bi-level optimization problem. A bi-level optimization model for grid-source-load coordinated operation was proposed in [27], where the upper-level problem minimizes system power purchase costs and the lower-level problem optimizes the overall economic performance of the VPP. A VPP scheduling model based on bi-level fuzzy chance-constrained programming was constructed in [28], and the interaction characteristics between the power grid and the VPP were revealed. A bi-level model based on time-of-use tariffs was established in [29], where the upper level mitigates wind and photovoltaic output fluctuations, and the lower level optimizes distribution network operational benefits. The interactive operation capability between VPPs and power grids has been enhanced by these studies, which also provide support for regional power supply–demand balance. In most existing VPP scheduling studies, electric vehicles are treated as equivalent to stationary energy storage systems, and the heterogeneity in user response reliability between orderly charging and vehicle-to-grid (V2G) discharging modes is rarely distinguished. This oversight makes it difficult to accurately characterize scheduling execution risks in vehicle–grid interaction scenarios.

In summary, existing studies on VPP scheduling generally take economic revenue maximization as the core objective and implicitly assume that all internal resources can respond to dispatch instructions with perfect reliability. However, heterogeneous demand-side resources differ significantly in terms of communication infrastructure, response speed, and scheduling execution capability, leading to non-negligible disparities in scheduling success probability. Neglecting these disparities yields overly optimistic scheduling schemes and causes deviations between actual execution performance and theoretical expectations, which may even impede improvements in renewable energy accommodation efficiency.

To address this research gap, a two-stage optimal scheduling method for VPPs, which considers the scheduling success probability of multi-agent generalized demand-side resources, is proposed in this paper. The principal contributions of this work are summarized as follows:

First, a quantitative model for the scheduling success probability of demand-side resource agents is established. The model characterizes scheduling failure risks arising from communication delays and untimely responses from two dimensions—relative capacity weight and dispatch response failure probability—thereby realizing quantitative coupling between communication uncertainty and economic scheduling decisions. Differentiated modeling is performed for the orderly charging and V2G modes of electric vehicles.

Second, a two-stage VPP optimal scheduling model based on a leader–follower game framework is constructed. In the first stage, the internal dispatch price is determined by the VPP; in the second stage, the schedulable capacity of each resource agent is optimized, with full consideration given to the independent decision-making autonomy and interest demands of individual agents.

Third, the backward induction method is adopted to decouple the two-stage problem, and the optimal dispatch price is rigorously derived via the Karush–Kuhn–Tucker (KKT) conditions. Case study results verify that the proposed method can effectively improve the overall revenue of VPPs and increase the renewable energy accommodation rate, providing technical support for the efficient and stable operation of VPPs.

2. Proposed Scheduling Model

In this section, a two-stage optimal scheduling model for VPPs that incorporates the scheduling success probability of multi-agent generalized demand-side resources is developed, aimed at mitigating dispatch inefficiency induced by heterogeneous response capabilities and communication uncertainties among distributed entities.

Within the proposed modeling framework, both the VPP operator and all resource agents are treated as rational economic entities pursuing net revenue maximization, with fully symmetric information assumed for all internal market parameters. The scheme submission process of each agent is modeled as a Poisson arrival process, where the inter-arrival time follows an exponential distribution, while key communication parameters—including channel capacity and coding gain—are maintained constant throughout a single scheduling cycle. A price-driven dispatch mechanism is employed: a unified internal dispatch price is first determined and announced by the VPP, based on which each resource agent optimizes its schedulable capacity within its feasible operating envelope. Forecasts of renewable generation and base load over the scheduling horizon are taken as given inputs. Emphasis is placed on internal dispatch coordination, and transient power constraints of the external distribution network are not included in the model formulation.

2.1. Scheduling Success Probability of Resource Agents

The actual effectiveness of demand-side resource agents participating in VPP dispatch is determined by two core attributes: first, the scale of their schedulable capacity, which determines their priority in dispatch allocation; second, the timeliness of scheme reporting and command response, which determines the execution reliability of dispatch instructions. This section quantifies these two independent dimensions—relative capacity weight and dispatch execution reliability—to establish the relationship between schedulable capacity and actual effective contribution.

For each generalized demand-side resource agent, its influence on internal dispatch allocation is positively correlated with its own schedulable capacity scale. The relative capacity weight is defined as the ratio of an individual agent's schedulable capacity to the total schedulable capacity of all generalized demand-side resources within the VPP, expressed as follows:

$$w_i = \frac{c_i}{\sum_{j \in I} c_j} \tag{1}$$

where w_i is the relative capacity weight of the i generalized demand-side resource agent, c_i is the schedulable capacity of resource agent i, and I is the set of all generalized demand-side resource agents within the VPP. By definition, the relative capacity weights satisfy the normalization property $\sum_{i \in I} w_i = 1$, and $w_i > 0$ for all agents.

The relative capacity weight is an allocation weight, and its value changes dynamically with the reported capacities of each agent. When other agents increase their reported capacities, the relative weight of a given agent decreases accordingly, reflecting the coupling characteristics of scale-based influence.

During VPP operation, each resource agent submits its dispatch scheme to the dispatch center through dedicated information exchange channels. Delays in scheme reporting or untimely command responses can reduce dispatch efficiency and may even exclude the agent from the current dispatch cycle, a situation defined as dispatch service request failure.

https://doi.org/10.3390/wevj17090484

To characterize the impact of communication delay on dispatch execution performance, the scheme submission process of each resource agent is modeled as a Poisson arrival process. The number of successful scheme submissions within a unit time interval follows a Poisson distribution, and the inter-arrival time between consecutive submission attempts—that is, the actual reporting delay—follows an exponential distribution with probability density function $f_X(x) = (1/T)\exp(-x/T)$ \ for $x \geq 0$, where T denotes the expected effective transmission duration of the dedicated communication link. Let Δ_{rel} denote the relative reporting delay beyond the inherent baseline Δ_{rel}, i.e., the additional delay induced by a nonzero data payload. Based on the cumulative distribution function of the exponential delay distribution, an exponential risk-function form is adopted to quantify the dispatch response failure probability as a monotone function of the relative delay:

$$P_{f,i} = 1 - \exp\left(-\frac{\Delta t_i}{T}\right) \tag{2}$$

$$\Delta t_i = t_i - t_0 \tag{3}$$

$$t_i \approx t_0 + \left.\frac{dt}{dD}\right|_{D_i=0} \cdot D_i \tag{4}$$

where D_i is the data volume of the dispatch scheme reported by resource agent i; T is the expected effective transmission duration of the communication system. Δt_i is the relative reporting delay corresponding to data volume D_i, defined as the difference between the actual reporting time and the inherent baseline communication delay; t_i is the total transmission delay corresponding to data volume D_i; and t_0 is the inherent baseline communication delay under zero payload. The first-order Taylor expansion of t_i at $D_i = 0$ yields Equation (4).

According to the Shannon–Hartley theorem, the data transmission rate is jointly determined by channel capacity and coding gain; therefore, the marginal transmission delay at zero payload satisfies:

$$\left.\frac{dt}{dD}\right|_{D=0} = \frac{1}{G_1 G_2} \tag{5}$$

where G_1 is the channel capacity of the data transmission link, and G_2 is the coding gain of the communication system. Substituting Equation (4) into Equation (3), the relative reporting delay can be further simplified as a linear function of data volume:

$$\Delta t_i = \frac{D_i}{G_1 G_2} \tag{6}$$

Substituting Equation (6) into Equation (2), the relative reporting delay Δ_{rel} is shown to be a linear function of the data volume D_i, whereas the dispatch response failure probability is a nonlinear function of D_i, specifically $P_{f,i} = 1 - \exp[-D_i/(G_1 G_2 T)]$. Accordingly, the dispatch execution reliability is the complement of the failure probability:

$$r_i = 1 - P_{f,i} = \exp\left(-\frac{D_i}{G_1 G_2 T}\right) \tag{7}$$

The execution reliability r_i is a strict probability metric, determined solely by the agent's own communication parameters and data volume, independent of the reported capacities of other agents.

To avoid ambiguity, three related but distinct terms are used consistently hereafter. "Scheduling success probability" is the framework-level concept that an assigned regulation task is executed successfully. "Dispatch execution reliability" is its per-agent probability measure. "Effective dispatch contribution coefficient" is the product of the relative capacity weight and the execution reliability, and is the only quantity used to allocate dispatch tasks.

Probabilistic interpretation of Equations (2) and (7). The exponential law in Equation (2) admits an exact probabilistic interpretation, rather than being merely an empirical risk-function form. The number of transmission opportunities provided by the dedicated channel within one dispatch cycle follows a Poisson process; by the Poisson–exponential equivalence, the effective service margin X is exponentially distributed with mean T, i.e., $f_{X(x)} = (1/T)exp(-x/T),\ x \geq 0$. Transmitting a payload D_i in turn requires the deterministic extra service time $\Delta t_i = \frac{D_i}{G_1 G_2}$ given by Equation (6). A report succeeds exactly when the available margin covers this required time, i.e., on the event $\{X \geq \Delta t_i\}$. The exponential survival function is precisely the execution reliability in Equation (7), while its complement is the failure probability in Equation (2). Equations (2) and (7) are therefore exact probabilities—a survival function and its complement—bounded in [0, 1] and strictly monotone: the execution reliability decreases with the payload D_i and increases with the channel capacity G_1, the coding gain G_2, and the effective margin T. The Poisson/exponential description is a standard traffic model for grid communication networks [30], and the adopted G_1 = 10 Mbps, G_2 = 1.2, and T = 0.5 s are consistent with dedicated power-communication channels: hard real-time protection messages form a different service class, whereas day-ahead dispatch-scheme reports are medium/low-speed transactions for which the permissible latency extends to the order of 10^2–10^3 ms. The sensitivity of the execution reliability to these communication parameters is examined in the case study. The channel parameters G_1, G_2, and T are taken from the configuration of the same demonstration-project private network, and the memoryless exponential law is the conservative choice because, at a fixed mean arrival rate, it is the maximum-entropy inter-arrival law.

The dispatch execution reliability $P_{s,i}$ quantifies the probability of successful command response. The relative capacity weight $w_i = c_i / \sum_j c_j$ reflects the agent's share in total schedulable capacity. For the Stage 2 follower problem, the effective response capacity is $P_{s,i} c_i$. The capacity weight w_i is retained at the VPP aggregation level for dispatch task allocation. The composite effective contribution coefficient at the VPP level is as follows:

$$\eta_i = w_i \cdot r_i \tag{8}$$

From a physical perspective, the relative capacity weight reflects the agent's inherent response capability and dispatch priority—larger-capacity agents are typically equipped with more advanced communication interfaces and dispatch execution facilities, corresponding to higher execution reliability—while the execution reliability reflects the timeliness of information exchange. Their product characterizes the combined effect of execution capability and transmission reliability on the final dispatch effectiveness. As shown in the above equation, the effective dispatch contribution coefficient is positively correlated with the agent's schedulable capacity and negatively correlated with the reported data volume. For the EV agent, the effective contribution coefficient is further modulated by the dual-mode user response reliability parameters in Equation (9), reflecting the higher execution risk associated with V2G discharging relative to orderly charging.

For user-side mobile energy storage resources represented by electric vehicles, their participation in VPP dispatch includes two typical operating modes: orderly charging and V2G discharging, with significantly different user response compliance between these two modes. A composite user response reliability coefficient is introduced to incorporate the performance differences in the dual modes:

$$R_{\mathrm{EV}} = m r_{\mathrm{oc}} + (1-m) r_{\mathrm{v2g}} \tag{9}$$

where m is the ratio of orderly charging capacity to the total adjustable capacity of the EV fleet; r_{oc} and r_{v2g} are the user response reliability coefficients under orderly charging and V2G discharging modes, respectively, satisfying $0 \le r_{\mathrm{oc}}$ and $r_{\mathrm{v2g}} \le 1$. The composite execution reliability of the EV agent, accounting for both communication delay and user response compliance, is then $P_{s,\mathrm{EV}} = P_{s,\mathrm{base}} \cdot R_{\mathrm{EV}}$, where $P_{s,\mathrm{base}}$ is the communication execution reliability given by Equation (7).

Correspondingly, the effective dispatch contribution coefficient of the EV agent follows the same definition as Equation (8), with the execution reliability replaced by the composite execution reliability $P_{s,\mathrm{EV}}$:

$$\eta_{\mathrm{EV}} = w_{\mathrm{EV}} \cdot P_{s,\mathrm{EV}} = w_{\mathrm{EV}} \cdot P_{s,\mathrm{base}} \cdot \left[m r_{\mathrm{oc}} + (1-m) r_{\mathrm{v2g}} \right] \tag{10}$$

where $w_{\mathrm{EV}} = c_{\mathrm{EV}} / \sum_{j \in \Omega} c_j$ is the relative capacity weight of the EV agent defined in Equation (1). Equation (10) ensures that the capacity weight and the execution reliability are each applied exactly once, eliminating any double-counting of these factors.

Upon successful plan submission and compliance with VPP dispatch instructions, transaction revenue is accrued to the resource agent, and the corresponding dispatch costs are incurred. The net revenue of resource agent i is formulated as follows:

$$R_i(c_i) = (\rho_o + b_i - c_i^d) P_{s,i} c_i - \tfrac{1}{2} a_i c_i^2 - c_i^{\mathrm{V2G}} d_i^{\mathrm{V2G}} \tag{11}$$

where p_o denotes the per-unit regulation compensation price paid by the VPP to the agent; b_i denotes the per-unit endogenous additional benefit obtained by the agent through dispatch participation; c_i^d represents the per-unit baseline dispatch cost incurred by the agent for participating in VPP dispatch; $P_{s,i} = \exp(-\Delta_{\mathrm{rel},i} / T)$ is the dispatch execution reliability derived in Equation (7); c_i is the declared schedulable capacity of agent i; $a_i > 0$ is the quadratic dispatch cost coefficient capturing the increasing marginal cost associated with larger capacity declarations, including accelerated battery degradation, reduced user comfort for controllable loads, and higher coordination overhead for the aggregator; c_i^{V2G} is the battery cycle degradation cost per unit of V2G discharged energy; and d_i^{V2G} is the V2G discharge power. The V2G degradation term is active only under the V2G discharging mode; under the orderly charging mode, the battery degradation cost is already included in the baseline dispatch cost c_i^d. This setup enables the V2G discharging decision to naturally balance regulation benefits against battery life degradation, thereby avoiding excessive calling. Two-layer role of the V2G degradation term. At the strategic-capacity layer, d_i^{V2G} is the V2G discharge energy produced by the multi-period dispatch under the declared-capacity cap c_i, and is treated as exogenous when optimizing c_i; it therefore does not enter the first-order condition in Equation (47). Degradation nevertheless affects the capacity decision indirectly, through the agent's net revenue Equation (11) and the individual-rationality threshold in Equations (15) and (16), and it is bounded at the multi-period layer by the degradation term in the EV energy balance Equation (22) and by the cumulative cycle-life constraint Equation (38). Thus, degradation shapes both the incentive to declare capacity and the realized discharge profile, without requiring d_i^{V2G} to be an explicit function of c_i in the closed-form best response.

Correspondingly, the VPP obtains regulation service revenue from the external electricity market by aggregating the effective response capacities of all agents and incurs compensation payments and aggregation management costs. The net revenue of the VPP is formulated as follows:

$$R_{\mathrm{VPP}}(\rho_o) = \sum_{i\in\Omega}\left(\lambda - \rho_o - c_i^{\mathrm{agg}}\right)P_{s,i}c_i \tag{12}$$

where λ denotes the per-unit regulation service revenue obtained by the VPP from the external market; c_i^{agg} denotes the per-unit aggregation cost of generalized demand-side resources borne by the VPP operator; and $P_{s,i}c_i$ is the effective response capacity of agent i after accounting for communication execution reliability. The relative capacity weight $w_i = c_i / \sum_{j\in\Omega} c_j$ is used in Section 4 to characterize each agent's share in the aggregate effective capacity and its contribution to total VPP revenue.

The relative capacity weight is jointly determined by the declared capacity of all agents. When other agents adjust the declared capacity, the weight of this agent will change accordingly. This characteristic is an inherent attribute of the scale allocation mechanism, which reflects the dynamic reallocation of relative bargaining influence among agents, and is essentially different from the execution reliability determined only by their own attributes.

2.2. Two-Stage Scheduling Model

The scheduling interaction between the VPP and multi-agent demand-side resources exhibits a canonical leader–follower decision-making structure. The internal dispatch price is determined by the VPP acting as the leader, while the schedulable capacity of each resource agent, functioning as the follower, is adjusted in response to the transmitted price signal. This interactive decision-making process is formulated as a two-stage optimization problem, in which the first-stage pricing decision and the second-stage capacity decision are mutually coupled.

In the first stage, the VPP determines the optimal internal dispatch price to maximize its net revenue obtained from aggregating demand-side resources. Since the schedulable capacity of each agent is endogenously determined by the second-stage optimization, the optimal capacity response function of the agents is embedded into the first-stage objective function. The corresponding optimization problem is formulated as follows:

$$\max_{\rho_o} R_{\mathrm{VPP}}(\rho_o) = \sum_{i\in\Omega}\left(\lambda - \rho_o - c_i^{\mathrm{agg}}\right)P_{s,i}c_i^*(\rho_o) \tag{13}$$

$$\begin{aligned} \text{s.t.} \quad & p_0^{\min} \le p_0 \le p_0^{\max} \\ & c_i^*\left(p_0\right) \in \Omega_i, \quad \forall i \in I, \\ & Q_i^{\mathrm{DSR}}\left(c_i^*\left(p_0\right)\right) \ge Q_i^{\mathrm{base}}, \quad \forall i \in I. \end{aligned} \tag{14}$$

where $p_0^{\min}$ and $p_0^{\max}$ denote the lower and upper bounds of the internal dispatch price as stipulated by market rules, respectively; $c_i^*\left(p_0\right)$ represents the optimal schedulable capacity response of resource agent *i* for a given dispatch price; Ω_i denotes the feasible capacity set of resource agent *i*; and Q_i^{base} corresponds to the benchmark revenue of resource agent *i* under independent operation, i.e., the reservation utility of the agent. The first constraint serves as the capacity feasibility constraint. The second is the individual rationality constraint, by which agents are guaranteed sufficient incentive to participate in VPP dispatch. The third constitutes the price boundary constraint. Substituting the Stage 2 optimal capacity in Equation (49) into the net revenue function in Equation (11), the maximum net revenue of agent *i* at a given price ρ_o is $R_i(c_i^*) = \dfrac{1}{2a_i}(\rho_o + b_i - c_i^d)^2 P_{s,i}^2 - c_i^{\mathrm{V2G}} d_i^{\mathrm{V2G}}$. The individual rationality constraint $R_i(c_i^*) \ge R_i^0$ is therefore satisfied when $\rho_o \ge \dfrac{\sqrt{2a_i(R_i^0 + c_i^{\mathrm{V2G}} d_i^{\mathrm{V2G}})}}{P_{s,i}} - b_i + c_i^d$. In the case study, the lower bound of the feasible price band exceeds this threshold for all resource agents, so the individual rationality constraint is automatically satisfied throughout the tested price range.

In the second stage, the dispatch price signal released by the VPP is received by each resource agent, and its optimal schedulable capacity within the feasible operating envelope is determined to maximize individual net revenue. Using the unified revenue function in Equation (11), the optimization problem for agent *i* is formulated as follows:

$$\max_{c_i} R_i(c_i) = (\rho_o + b_i - c_i^d)P_{s,i}c_i - \frac{1}{2}a_i c_i^2 - c_i^{\mathrm{V2G}} d_i^{\mathrm{V2G}} \tag{15}$$

$$\begin{aligned} \text{s.t.} \quad & p_0^{\min} \le p_0 \le p_0^{\max} \\ & c_i^*\left(p_0\right) \in \Omega_i, \quad \forall i \in I, \\ & Q_i^{\mathrm{DSR}}\left(c_i^*\left(p_0\right)\right) \ge Q_i^{\mathrm{base}}, \quad \forall i \in I. \end{aligned} \tag{16}$$

where $c_i^{\min}$ and $c_i^{\max}$ denote the lower and upper bounds of the schedulable capacity of resource agent *i*, respectively. The constraints are presented in the following order: the schedulable capacity boundary constraint, the probability value validity constraint, the communication parameter feasibility constraint, and the individual rationality constraint.

It can be demonstrated that $R_i(c_i)$ is concave with respect to c_i for each individual agent. This property guarantees that the first-order optimality condition is both necessary and sufficient for the global optimal solution of each agent's Stage 2 subproblem, and no local optimum trap is encountered at the individual agent level. In the subsequent derivation, the capacity boundary constraint is addressed via a projection operation, while the individual rationality constraint is verified through numerical comparison in the case study. Accordingly, the candidate optimal solution is first derived from the first-order condition at interior points, and then projected onto the feasible capacity interval to yield the final optimal schedulable capacity.

2.3. Physical Constraints of Multi-Period Operation

The schedulable capacity c_i determined by the Stackelberg game in Section 2.2 serves as the capacity upper bound for the multi-period operational variables of each resource agent. Specifically, for each agent $i \in \Omega$, the hourly operational power is constrained by $\max_{t \in T_i} P_i^{\mathrm{op}}(t) \le c_i$, where $P_i^{\mathrm{op}}(t)$ denotes the operational power of agent *i* at period *t*—the charge–discharge power for energy storage and EV agents, the load adjustment relative to baseline consumption for air-conditioning loads, and the dispatched output for renewable energy agents—and T_i denotes the set of available periods for agent *i*. This linking constraint explicitly connects the strategic capacity variable from the game-theoretic layer to the hourly operational variables in the multi-period layer, ensuring that both layers form a coherent optimization framework: the game layer determines the capacity allocation among agents, while the multi-period layer determines the temporal distribution of each agent's allocated capacity subject to the physical constraints presented below.

Reliability-weighted allocation of multi-period dispatch tasks. Once the Stackelberg game settles the declared schedulable capacity c_i^* of every agent, the multi-period layer distributes the system-wide regulation task of each period among the agents that are available in that period. Let $F_t \subseteq \Omega$ denote the set of agents online at period *t*, and let F_t be the net regulation task at period *t* (positive for discharging/load reduction and negative for charging/renewable absorption). To prevent dispatch tasks from being concentrated on agents that declare a large capacity but respond unreliably, each agent is assigned a dispatch-share weight built from its effective dispatch contribution coefficient η_i defined in Equation (8). And its target operational task is allocated proportionally:

$$\beta_i = \eta_i = w_i \; P_{s,i} \tag{17}$$

$$\alpha_{\{i,t\}} = \beta_i \,/\, \Sigma_{\{j \in F\_t\}} \beta_j \tag{18}$$

$$P_i^{op}(t) = \alpha_{\{i,t\}} \; L_t \tag{19}$$

Before being projected onto the feasible operational set $\Phi_{\{i,t\}}$ defined by the capacity envelope together with the physical constraints (21)–(46),

$$P_i^{op}(t) = \prod\nolimits_{\Phi_{\{i,t\}}} [P_i^{op}(t)] \tag{20}$$

Here $\prod_{\Phi_{\{i,t\}}}[\cdot]$ denotes projection onto $\Phi_{\{i,t\}}$. Equation (20), together with the power balance in Equation (21), closes the multi-period layer.

Layered role of the relative capacity weight. The two decision layers must be distinguished. In Stage 2, a follower chooses its own declared capacity c_i by maximizing Equation (11); at this point, no task is yet shared among agents, so the first-order condition in Equation (45) depends solely on the agent's own execution reliability $P_{s,i}$ and intentionally does not contain w_i. The relative capacity weight, which couples agents through $w_i = c_i / \Sigma_j c_j$, acts at the layer above, namely, the VPP-level multi-period allocation in Equations (17)–(20), where the settled capacities are shared out as hourly operational tasks. Therefore w_i is neither a post-processing indicator nor absent from the optimization: it shapes the hourly dispatch profile $P_i^{op}(t)$, and through it the renewable accommodation, the peak–valley difference, and the realized revenue. This is precisely why the three scenarios differ. Under Scenario 1, the share weight is $\beta_i = w_i P_{s,i}$; under Scenario 3, the capacity-weight factor is removed and $\beta_i = P_{s,i}$; under Scenario 2, execution is assumed perfectly reliable and the task is shared equally.

Power conservation at all time periods constitutes the core constraint of the scheduling scheme:

$$\begin{aligned}&P_{w,t} + P_{pv,t} + P_{dis,ess,t} + P_{dis,ev,t} + P_{grid,buy,t} = \\ &P_{ac,t} + P_{ch,ess,t} + P_{ch,ev,t} + P_{grid,sell,t} + P_{cur,w,t} + P_{cur,pv,t} \quad \forall t\end{aligned} \tag{21}$$

where $P_{w,t}$ and $P_{pv,t}$ are the forecasted available outputs of wind power and photovoltaic (PV) at time period t; $P_{dis,ess,t}$ and $P_{ch,ess,t}$ are the discharging and charging power of the energy storage battery; $P_{dis,ev,t}$ and $P_{ch,ev,t}$ are the V2G discharging and orderly charging power of the electric vehicle (EV) fleet; $P_{ac,t}$ is the actual power consumption of air-conditioning loads; $P_{grid,buy,t}$ and $P_{grid,sell,t}$ are the power purchased from the grid and sold to the grid by the VPP; and $P_{cur,w,t}$ and $P_{cur,pv,t}$ are the curtailment power of wind power and photovoltaic.

A dynamic recursive model of SOC considering charge and discharge efficiency is adopted:

$$E_{ess,t+1} = E_{ess,t} + \eta_{ch,ess} P_{ch,ess,t} \Delta t - \frac{P_{dis,ess,t}}{\eta_{dis,ess}} \Delta t \quad \forall t \tag{22}$$

where $E_{ess,t}$ is the stored energy of the energy storage at the beginning of time period t, and $\eta_{ch,ess}$ and $\eta_{dis,ess}$ are the charging and discharging efficiencies, respectively. The SOC boundary constraints, along with the initial and terminal SOC constraints, ensure energy neutrality over the dispatch horizon, and 0–1 state variables are introduced to prevent simultaneous charging and discharging.

$$E_{ess,\min} \le E_{ess,t} \le E_{ess,\max} \quad \forall t \tag{23}$$

$$E_{ess,1} = E_{ess,\text{init}} \tag{24}$$

$$E_{ess,25} = E_{ess,\text{end}} \tag{25}$$

$$P_{ch,ess,t} \le u_{ess,t} P_{ch,ess,\max} \quad \forall t \tag{26}$$

$$P_{dis,ess,t} \le (1-u_{ess,t}) P_{dis,ess,\max} \quad \forall t \tag{27}$$

$$u_{ess,t} \in \{0,1\} \quad \forall t \tag{28}$$

A dynamic availability model is adopted for electric vehicles across periods, relaxing the fixed-capacity assumption, including charging and discharging efficiency and degradation loss:

$$E_{ev,t+1} = E_{ev,t} + \eta_{ch,ev} P_{ch,ev,t} \Delta t - \frac{P_{dis,ev,t}}{\eta_{dis,ev}} \Delta t \quad \forall t \tag{29}$$

where $\eta_{ch,ev}$ and $\eta_{dis,ev}$ are the charging and V2G discharging efficiencies, respectively.

Grid-connected periods and dynamic availability constraints: the EVs can only participate in dispatch during grid-connected periods, with power set to zero during off-grid periods. Let the arrival time of the vehicle fleet be denoted as t_{arr} and the departure time as t_{dep}:

$$P_{ch,ev,t} = 0, \quad P_{dis,ev,t} = 0 \quad \forall t \notin [t_{arr}, t_{dep}] \tag{30}$$

Since the grid-connected window spans midnight, the availability set is explicitly partitioned into two intervals: $t \in [19,24] \cup [0,7]$. During the off-grid periods $t \in [7,19]$, both the orderly charging power and the V2G discharging power of the EV fleet are enforced to zero, as the vehicles are disconnected from the VPP and unavailable for dispatch. This time-varying availability constraint is embedded directly into the multi-period optimization, ensuring that no EV power is scheduled outside the physically feasible grid-connected window.

The maximum charge and discharge power in each period changes dynamically with the real-time SOC, and there is no fixed adjustable capacity all day. The off-grid minimum power constraint to ensure users' travel needs is as follows:

$$E_{ev,t_{dep}+1} \ge E_{ev,\text{min,dep}} \tag{31}$$

where $E_{ev,\text{min,dep}}$ is the minimum state-of-charge energy required at the time of departure. The initial state-of-charge constraints and the charging/discharging mutual exclusivity constraints are as follows:

$$E_{ev,t_{arr}} = E_{ev,\text{init}} \tag{32}$$

$$P_{ch,ev,t} \le u_{ev,t} P_{ch,ev,\max} \quad \forall t \tag{33}$$

$$P_{dis,ev,t} \le (1-u_{ev,t}) P_{dis,ev,\max} \quad \forall t \tag{34}$$

$$u_{ev,t} \in \{0,1\} \quad \forall t \tag{35}$$

The battery cycle life constraint is as follows: limit the cumulative charge and discharge throughput in the scheduling period and avoid the accelerated aging of the battery caused by excessive V2G.

$$\sum_{t=1}^{24}\left(P_{ch,ev,t}+P_{dis,ev,t}\right)\Delta t \le E_{ev,\mathrm{put,max}} \tag{36}$$

An equivalent thermal parameter model is employed to describe indoor temperature dynamics:

$$T_{in,t+1}=T_{in,t}+\frac{1}{C_{th}}\left(\frac{T_{in,t}-T_{out,t}}{R_{th}}-P_{ac,t}\cdot COP\right)\Delta t \quad \forall t \tag{37}$$

where $T_{in,t}$ is the indoor temperature, $T_{out,t}$ is the outdoor ambient temperature, C_{th} is the equivalent thermal capacity of the building, R_{th} is the equivalent thermal resistance of the building, and COP is the coefficient of performance of the air-conditioning system. The user comfort constraints are as follows:

$$T_{in,\min} \le T_{in,t} \le T_{in,\max} \quad \forall t \tag{38}$$

The actual consumed power does not exceed the predicted output, and the abandoned power is non-negative:

$$0 \le P_{cur,w,t} \le P_{w,t} \quad \forall t \tag{39}$$

$$0 \le P_{cur,pv,t} \le P_{pv,t} \quad \forall t \tag{40}$$

The formula for calculating the renewable energy consumption rate is as follows:

$$\text{A rate}=\frac{\sum_{t=1}^{24}(P_{w,t}-P_{cur,w,t}+P_{pv,t}-P_{cur,pv,t})}{\sum_{t=1}^{24}(P_{w,t}+P_{pv,t})}\times 100\% \tag{41}$$

Mutually exclusive constraints for power purchase and sale, together with power limit constraints, are imposed:

$$P_{grid,buy,t} \le u_{grid,t}P_{grid,\max} \quad \forall t \tag{42}$$

$$P_{grid,sell,t} \le (1-u_{grid,t})P_{grid,\max} \quad \forall t \tag{43}$$

$$u_{grid,t} \in \{0,1\} \quad \forall t \tag{44}$$

Time-of-use pricing mechanism $c_{buy,t}$ is the unit electricity purchase price at time period *t*, and $c_{sell,t}$ is the unit electricity sale price at time period *t*, with differentiated values for peak, flat, and off-peak periods. The grid interaction cost is included in the total operating cost of the VPP.

All equipment variables are subject to physical upper and lower bounds:

$$0 \le P_{ac,t} \le P_{ac,\max} \quad \forall t \tag{45}$$

$$0 \le P_{grid,buy,t}, P_{grid,sell,t} \le P_{grid,\max} \quad \forall t \tag{46}$$

https://doi.org/10.3390/wevj17090484

3. Solution by Backward Induction

The established two-stage scheduling model exhibits the canonical sequential decision-making structure of a Stackelberg game. The dispatch price is set by the VPP acting as the leader, while the schedulable capacity of each resource agent, functioning as followers, is adjusted accordingly. To obtain the subgame-perfect equilibrium of this bi-level decision problem, the backward induction method is employed for the solution. As a standard approach for dynamic game analysis and bi-level optimization, backward induction first derives the followers' optimal response to a given leader decision, and then substitutes the response function into the leader's optimization problem to yield the globally optimal decision. The derivations of the optimal capacity response in Stage 2 and the optimal pricing strategy in Stage 1 are elaborated below. As a canonical solution paradigm for Stackelberg dynamic games, backward induction guarantees a subgame-perfect equilibrium and effectively eliminates non-credible threats inherent in sequential decision-making.

3.1. Optimal Capacity Response in Stage 2

For a given internal dispatch price ρ_o, the optimal schedulable capacity of each resource agent is determined by maximizing the net revenue function in Equation (15). Since $P_{s,i}$ is independent of c_i (it is determined solely by the agent's communication parameters and data volume via Equation (7)), the first-order derivative of $R_i(c_i)$ with respect to c_i is as follows:

For a given internal dispatch price ρ_o, each resource agent determines its optimal schedulable capacity by maximizing the net-revenue function in Equation (15). In taking the derivative with respect to c_i, two terms are independent of c_i: $P_{s,i}$, which is fixed solely by the agent's communication parameters and data volume through Equation (7), and the V2G discharge energy d_i^{V2G}, which is the execution quantity produced by the multi-period physical dispatch under the declared-capacity cap and is hence exogenous to c_i at this strategic layer. The first-order derivative of R_i (c_i) with respect to c_i is therefore:

$$\frac{\partial R_i}{\partial c_i} = (\rho_o + b_i - c_i^d)P_{s,i} - a_i c_i \tag{47}$$

Note that w_i does not appear in Equation (47): a Stage 2 follower declares its capacity before multi-period tasks are shared, and the coupling induced by w_i is exercised only at the VPP allocation layer through Equations (17)–(20). The second-order derivative is as follows:

$$\frac{\partial^2 R_i}{\partial c_i^2} = -a_i < 0 \tag{48}$$

Equation (48) confirms that R_i is strictly concave in c_i, so the first-order optimality condition is both necessary and sufficient for the unique global maximum. Setting Equation (47) to zero yields the candidate optimal interior solution:

$$c_i^* = \frac{(\rho_o + b_i - c_i^d)P_{s,i}}{a_i} \tag{49}$$

When the upper and lower bounds of schedulable capacity are taken into account, the candidate interior solution is projected onto the feasible capacity interval:

$$c_i^* = \max\left(c_i^{\min}, \min\left(c_i^{\max}, \frac{(\rho_o + b_i - c_i^d)P_{s,i}}{a_i}\right)\right) \tag{50}$$

A grid-search verification is performed over 1000 uniformly spaced capacity points within the feasible interval $[c_i^{\min}, c_i^{\max}]$ for a representative set of dispatch prices. The numerically identified maximizer matches the analytical solution in Equation (49) with a maximum relative deviation below 10^{-4}, and the strict concavity of $R_i(c_i)$ is confirmed by the unimodal revenue profile across all tested scenarios.

Interiority over the complete price band. Before substituting Equation (49) into the Stage 1 objective, we verify that the projection of Equation (50) is inactive on the entire admissible price band $\rho_o \in [\rho_o^{\min}, \rho_o^{\max}] = [200, 500]$ CNY/MWh, so that the unprojected interior expression used below is exact rather than approximate. From Equation (49), the best response $c_i^*(\rho_o) = (\rho_o + b_i - c_i^d)P_{s,i}/a_i$ is affine and strictly increasing in ρ_o, since its slope $P_{s,i}/a_i$ is positive; its extrema on the closed band are therefore attained at the two endpoints, and it suffices to check interiority at ϱomin and ϱomax. (i) At the lower endpoint, the individual-rationality analysis of Equations (15) and (16) shows that $\rho_o^{\min}$ exceeds every agent's participation threshold, so the optimal response is strictly positive and above the lower capacity bound for all agents. (ii) At the upper endpoint $\rho_o^{\max} = 500$ CNY/MWh, which is also the equilibrium price of the case study, a dense one-dimensional grid search over the capacity interval confirms that the numerical maximiser coincides with Equation (49) to within a relative error below 10^{-4} and that the net-revenue profile is strictly unimodal, i.e., $c_i^*(\rho_o^{\max})$ lies strictly below $c_i^{\max}$. By affine monotonicity, $c_i^{\min} < c_i^*(\rho_o) < c_i^{\max}$ holds for every agent and for every ϱo in the complete band [200, 500]. The projection of Equation (50) is consequently inactive throughout, and substituting the unprojected Equation (49) into the Stage 1 revenue to obtain the concave quadratic Equation (53) is exact. For completeness, if the price band was widened so that an agent's response reached a capacity bound, Equation (50) would hold that agent at the bound, and the leader objective would become a piecewise (still concave) quadratic, whose active segment is selected by the three KKT cases listed after Equation (55); the present case study lies entirely in the interior regime and never enters this piecewise regime.

When the optimal response functions of all resource agents are solved simultaneously, a Nash equilibrium schedulable capacity profile is obtained for the given dispatch price, which constitutes the input to the VPP's pricing decision in Stage 1.

3.2. Optimal Dispatch Price in Stage 1

When the equilibrium optimal capacities of all agents derived in Stage 2 are substituted into the VPP net revenue function, the original two-stage problem is reduced to a single-variable optimization problem with respect to ρ_o. Substituting Equation (49), $c_i^* = (\rho_o + b_i - c_i^d)P_{s,i}/a_i$, into Equation (12) and collecting terms by powers of ρ_o, define the following:

$$K = \sum_{i \in \Omega} \frac{P_{s,i}^2}{a_i},$$
$$C = \sum_{i \in \Omega} \frac{P_{s,i}^2}{a_i} \left(\lambda - c_i^{\text{agg}} - b_i + c_i^d \right) \tag{51}$$
$$B = \sum_{i \in \Omega} \frac{P_{s,i}^2}{a_i} \left(\lambda - c_i^{\text{agg}} \right) \left(b_i - c_i^d \right)$$

The product term inside the summation is expanded as follows:

$$\left(\lambda - \rho_o - c_i^{\text{agg}} \right) \left(\rho_o + b_i - c_i^d \right) = \left(\lambda - c_i^{\text{agg}} \right) \left(b_i - c_i^d \right) + \left(\lambda - c_i^{\text{agg}} - b_i + c_i^d \right) \rho_o - \rho_o^2 \tag{52}$$

Substituting Equation (52) into the summation and collecting terms by powers of ρ_o yields the constants *K*, *C*, and *B* defined in Equation (51), and the VPP net revenue becomes the following:

$$R_{\text{VPP}}(\rho_o) = B + C\rho_o - K\rho_o^2 \tag{53}$$

Since $K > 0$, R_{VPP} is strictly concave in ρ_o, guaranteeing a unique maximum. Differentiating Equation (53) with respect to ρ_o yields the following:

$$\frac{dR_{\text{VPP}}}{d\rho_o} = C - 2K\rho_o \tag{54}$$

The unconstrained optimal price is obtained by setting Equation (54) to zero:

$$\rho_o^{\text{unc}} = \frac{C}{2K} \tag{55}$$

Under the inequality constraints $\rho_o^{\min} \le \rho_o \le \rho_o^{\max}$, the KKT conditions yield three cases: (i) if $\rho_o^{\min} < C/(2K) < \rho_o^{\max}$, the optimum is interior: $\rho_o^* = C/(2K)$; (ii) if $C/(2K) \le \rho_o^{\min}$, the optimum is at the lower bound: $\rho_o^* = \rho_o^{\min}$; (iii) if $C/(2K) \ge \rho_o^{\max}$, the optimum is at the upper bound: $\rho_o^* = \rho_o^{\max}$. Under the case-study parameters in Section 4, $C/(2K)$ falls at the upper bound of the feasible price band, so $\rho_o^* = \rho_o^{\max}$, consistent with the original numerical result.

It should be emphasized that the coincidence of the optimal price with the upper bound in this case study is a consequence of the specific economic parameters and feasible price band adopted herein, rather than a universal property of all two-stage VPP pricing problems. In general, the optimal price is determined by projecting the unconstrained optimum $C/(2K)$ onto the feasible interval, and an interior optimum may arise if the price band is widened or if the market revenue, aggregation cost, and quadratic cost parameters take different values. The scalability analysis in Section 4 confirms the computational efficiency of the proposed method for systems with up to 50 agents; extension to very-large-scale VPPs with hundreds or thousands of agents will require additional complexity analysis and is deferred to future work.

The overall solution architecture of the proposed two-stage scheduling model is depicted in Figure 1.

In accordance with the backward induction logic, the effective dispatch contribution coefficient of each resource agent is first computed based on basic input data. Subsequently, the Nash equilibrium capacity of each agent in Stage 2 is solved under a specified dispatch price, and the optimal dispatch price in Stage 1 is ultimately derived via the KKT conditions. The final outputs encompass the optimal scheduling scheme, total revenue, renewable energy accommodation rate, and additional operational performance metrics. Under the model assumptions and parameter settings of this paper, each agent has a unique optimal response in Stage 2 for a given dispatch price, and the Stage 1 objective function is strictly concave with respect to the dispatch price. Individual concavity alone does not constitute a formal proof of the uniqueness or stability of the coupled Nash equilibrium; such a proof would require additional conditions such as diagonal strict concavity, contraction of the best-response map, or a potential-game property. In the case study, the backward induction procedure numerically converges to a Stackelberg equilibrium, as verified in Section 4.3. A rigorous theoretical proof of general uniqueness and equilibrium stability conditions is deferred to future work.

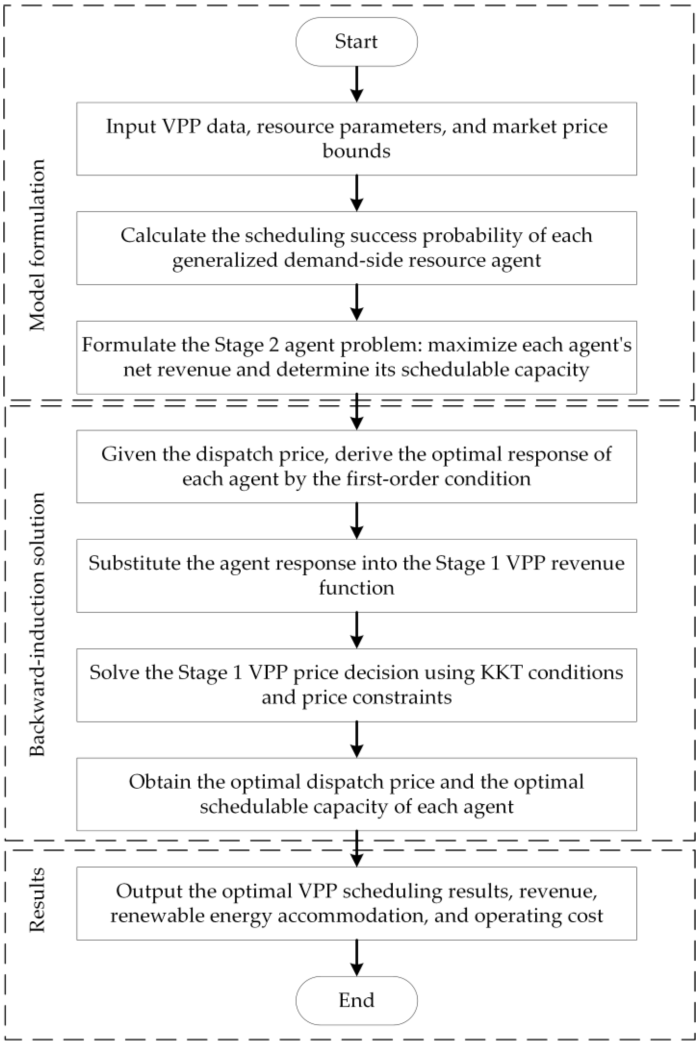

Figure 1. Sequential solution process of the two-stage VPP scheduling model based on backward induction.

4. Case Study

4.1. System Configuration and Simulation Setup

In this section, the basic parameters of the VPP system, the simulation environment, and the design of comparative scenarios are presented to ensure the reproducibility and methodological rigor of the case study. Five categories of generalized demand-side resources are integrated within the VPP system: wind turbines, photovoltaic units, battery energy storage systems, electric vehicles, and controllable air-conditioning loads.

The installed capacity and operational parameters of each resource type are configured based on practical engineering data. The rated capacity of wind turbines is set at 6 MW, and that of photovoltaic units at 8 MW. The battery energy storage system features a rated energy capacity of 10 MWh and a maximum charge–discharge power of 5 MW. The aggregated electric vehicle fleet has a total energy capacity of 8 MWh, with a maximum charge–discharge power of 4 MW. The scheduling horizon spans 24 h with a temporal resolution of 1 h.

Key economic and communication parameters are specified in accordance with the modeling framework established in Section 2. The permissible range of the internal dispatch price is defined as $p_o^{\min}$ = 200 and $p_o^{\max}$ = 500, which is aligned with the prevailing price band of demand response ancillary services in China.

The system parameters and load profiles are configured with reference to practical engineering data from a regional VPP demonstration project. The renewable output and load forecast curves are generated from historical measured data with a 1 h sampling resolution, processed via outlier removal and missing-value interpolation to produce the day-ahead forecast profiles shown in Figures 2 and 3. All simulation parameter values are fully listed in Tables 1 and 2 to ensure the reproducibility of the numerical results. The comparative analysis adopts an ablation-study design to isolate the individual contribution of the relative-capacity-weight dimension and the communication-reliability dimension; a direct comparison with existing VPP scheduling algorithms from the literature is deferred to future work.

Table 1. Effective dispatch contribution coefficient and economic parameters of VPP resource agents.

Resource Agent	Effective Dispatch Contribution Coefficient	Dispatch Cost (CNY/MWh)	Aggregation Cost (CNY/MWh)
Wind turbines	0.14	423	37
Photovoltaic units	0.16	315	24
Energy storage batteries	0.21	137	13
Air-conditioning loads	0.26	258	22
Electric vehicles	0.23	362	49

The quadratic dispatch cost coefficients are set to a_i = 0.8, 0.6, 1.2, 1.5, and 1.0 CNY/(MW^2·h) for the wind, photovoltaic, storage, EV, and air-conditioning agents, respectively. In Equation (11), $\frac{1}{2}a_i c_i^2$ is the convex dispatch cost term, so a_i is the rate at which the marginal dispatch cost $a_i c_i$ in Equation (47) rises with the declared capacity; its CNY/(MW^2·h) unit follows directly from dimensional consistency with the per-MWh price term $(\rho_o + b_i c_i^d)P_{s,i}$. The relative magnitudes reflect the physical and economic flexibility of each resource. The two renewables carry the smallest coefficients (PV 0.6, wind 0.8) because their near-zero variable generation cost makes additional declared capacity cheap; the controllable load is intermediate (1.0) because deeper regulation only trades off occupant comfort; battery resources carry larger coefficients (storage 1.2, EV 1.5) because declaring more capacity implies deeper cycling and faster degradation, with the EV largest because of its additional travel-uncertainty and V2G-compliance burden. The absolute scale is calibrated from the marginal-cost range observed in the regional VPP demonstration project and is consistent with the measured 125 CNY/MWh V2G cycling-degradation cost in Table 2. Interiority is not a calibration target but a post-calibration validity check, established analytically over the whole price band in Section 3.1. As a closed-form sensitivity check, Equation (49) gives the local elasticity $\partial ln\ c_i^* / \partial ln\ a_i = -1$: a common multiplicative perturbation of all a_i leaves the optimal-price ratio *C*/(2*K*) and the scenario ranking unchanged and scales all capacities and revenues by the same factor, while the interiority result of Section 3.1 continues to hold for perturbations within ±20% Parameters of the communication system are determined with reference to typical metrics of dedicated power communication networks: a channel capacity G_1 of 10 Mbps, a coding gain G_2 of 1.2, and an expected effective transmission duration *T* of 0.5 s. The cost parameters and effective dispatch contribution coefficient for each resource agent are detailed in Table 1. All baseline operational data are acquired from practical engineering projects, and the forecast curves are generated at a 1 h resolution as described above. The forecasted renewable generation profiles and load curves over the scheduling horizon are depicted in Figure 2 and Figure 3, respectively.

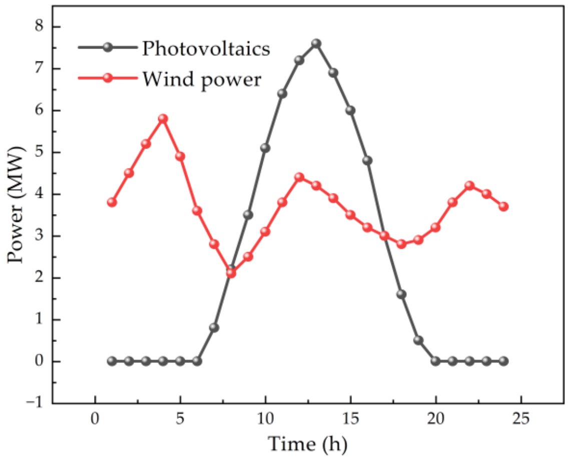

Figure 2. Predicted wind and photovoltaic output.

Figure 2 depicts the 24 h forecasted output profiles of wind and photovoltaic generation. Wind power exhibits a typical anti-peak characteristic: its output remains relatively high during nighttime and early morning and declines progressively after sunrise. By contrast, photovoltaic output is entirely concentrated in daytime hours (07:00–19:00) and attains a peak value of 7.6 MW at approximately 13:00. Such complementary output characteristics between wind and solar resources lay a fundamental basis for multi-resource coordination within the VPP.

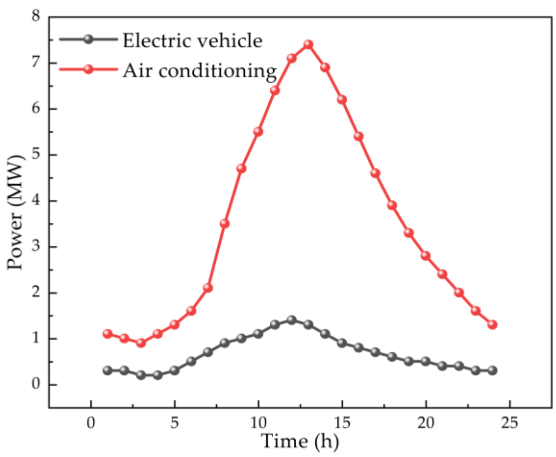

Figure 3. Predicted electric vehicle and air-conditioning load profiles.

https://doi.org/10.3390/wevj17090484

Figure 3 illustrates the forecasted load profiles of electric vehicles and air-conditioning loads. The air-conditioning load presents a pronounced single-peak distribution, with a peak of 7.4 MW emerging at 13:00, which is roughly synchronized with the peak photovoltaic output. In comparison, the electric vehicle load remains relatively flat, with a minor peak observed during commuting periods. The matching relationship between load peaks and renewable generation peaks constitutes the core basis for VPP demand response dispatch.

Table 2. Core parameters of multi-period operation.

Parameter Category	Parameter Symbol	Value	Parameter Symbol	Value
Energy Storage Battery	Charging efficiency	0.95	Discharging efficiency	0.93
	SOC operating range	10%~90%	Initial/Terminal SOC	50%
Electric Vehicles	Charging efficiency	0.92	V2G discharging efficiency	0.90
	Fleet arrival time	19:00	Fleet departure time	07:00 next day
	Initial SOC upon connection	30%	Minimum SOC upon departure	80%
	Unit discharging degradation cost	125 CNY/MWh	Daily throughput upper limit	12 MWh
Air-Conditioning Load	Equivalent thermal resistance	0.8 °C/kW	Equivalent thermal capacitance	12 kWh/°C
	Cooling COP	3.2	Comfort range	24~26 °C
Grid Interaction	Peak period purchase price	850 CNY/MWh	Off-peak purchase price	320 CNY/MWh
	Electricity sale price	450 CNY/MWh	Grid connection point power upper limit	10 MW

All numerical simulations are implemented in MATLAB R2023b on a workstation equipped with an Intel Xeon Gold 6346 CPU and 64 GB of RAM. The backward induction solution framework is independently coded. Each single-stage optimization subproblem is formulated via the YALMIP toolbox and solved by the CPLEX 12.10 solver. The convergence tolerance for the iterative solution of multi-agent equilibrium is set to 10^{-6}, and the maximum iteration number is specified as 100 to guarantee solution accuracy.

To quantitatively assess the contribution of the proposed scheduling success probability model, three comparative scenarios are designed under a controlled variable principle:

Scenario 1 (Proposed method): The scheduling success probability model, incorporating both the relative capacity weight and the dispatch response failure probability, is fully embedded into the two-stage optimization framework, and multi-period dispatch tasks are shared with the weight $\beta_i = w_i P_{s,i}$ in Equation (17).

Scenario 2 (Conventional method): The scheduling success probability is not taken into account, and all resource agents are assumed to respond to dispatch instructions with perfect reliability; communication delays and response uncertainties are neglected entirely, and the regulation task is shared equally among online agents.

Scenario 3 (Partial consideration): Only the communication failure probability is included in the model, while the relative capacity weight is not introduced into success-probability quantification; equivalently, the share weight in Equation (17) degenerates to $\beta_i = P_{s,i}$. This setup leads to a moderate overestimation of resource response capability, and the resulting net revenue falls between those of Scenario 1 and Scenario 2.

4.2. Core Scheduling Performance and Characteristic Analysis

Table 1 summarizes the effective dispatch contribution coefficient, per-unit dispatch cost, and per-unit aggregation cost of each resource agent under baseline conditions, all of which are calculated based on capacity scale and corresponding communication parameters.

The results reveal pronounced heterogeneity in the effective dispatch contribution coefficient across heterogeneous resources. A minimum value of 0.14 is recorded for wind turbines, while a maximum value of 0.26 is observed for air-conditioning loads, corresponding to a relative difference of 85.7%. This discrepancy is jointly governed by the geographical dispersion of resources and the magnitude of schedulable capacity, which provides a quantitative foundation for differentiated dispatch allocation in the subsequent optimization framework. For electric vehicle agents, the aggregated parameters are derived as weighted composites of the orderly charging and V2G discharging modes: orderly charging capacity accounts for 60% of the total adjustable capacity, while V2G capacity constitutes the remaining 40%. The two user-response compliance coefficients are estimated from the EV-aggregation dispatch records of the regional demonstration project, which log every dispatched instruction together with its mode and whether a response was delivered within the required deadline. For each mode, the compliance rate is the Bernoulli sample proportion of successful responses, $r_{\mathrm{mode}} = n_{\mathrm{success}}/n$, whose estimation uncertainty is bounded by a Wilson binomial interval and, conservatively, by the explicit ±0.05 parameter-band sensitivity reported in Section 4.3. Orderly charging, which follows an agreed timetable, attains a high fulfilment rate r_{oc} = 0.95, whereas V2G discharging, which additionally requires real-time consent and is discouraged by range anxiety and battery-wear concerns, has a lower fulfilment rate r_{V2G} = 0.75. This systematic ordering—discharge compliance below charge compliance and requiring stronger compensation—is consistent with reported EV-aggregator response-willingness studies [31,32].

These coefficients are fleet-level conditional expected response probabilities over the scheduling horizon. With ζ denoting the driver state, the strategic-layer model uses the state-averaged rate $r_{\mathrm{mode}} = E_{\zeta}[r_{\mathrm{mode}}(\zeta)]$, which is the deterministic-equivalent input appropriate to the day-ahead capacity game and is unbiased for expected revenue; the state dependence is not omitted but modeled at the operational time scale where it acts, through the time-varying grid-connection window, and through price in the objective. A fully state-dependent dynamic compliance model is left as future work. The sensitivity of the EV composite reliability to r_{oc} and r_{V2G} is analyzed in closed form in Section 4.3.

Table 2 lists the core parameters of the multi-period operation of this example, and the specific contents are as follows. Table 3 provides the values and definitions of core operation parameters of this example.

The overall effective dispatch contribution coefficient of electric vehicle agents is depressed by the inclusion of the V2G mode. When only the orderly charging mode is considered, the corresponding effective dispatch contribution coefficient reaches 0.26, a level comparable to that of air-conditioning loads. This finding further corroborates the high-risk nature of V2G discharging in scheduling execution.

Figure 4 decomposes the effective dispatch contribution coefficient into two constituent dimensions: relative capacity weight and execution reliability.

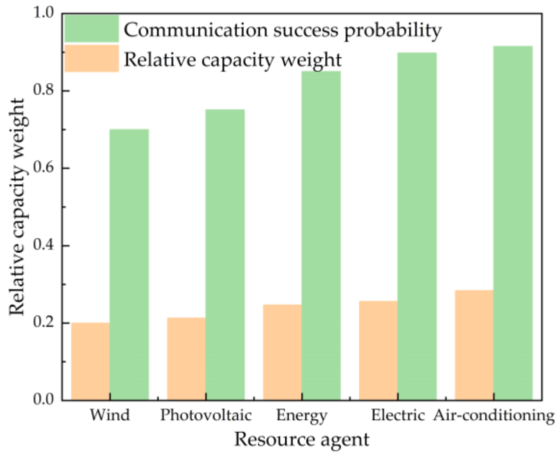

Figure 4. Decomposition of effective dispatch contribution coefficient for each resource agent.

In terms of execution reliability, a gap of 21.5 percentage points is observed between the highest and lowest values. With respect to the relative capacity weight, the difference between the maximum and minimum values is measured at 0.084. The final effective dispatch contribution coefficient of heterogeneous resources is jointly shaped by the product of these two dimensions.

For the relative capacity weight dimension, the highest weight of 0.284 is associated with air-conditioning loads, attributable to their largest aggregated schedulable capacity, while the lowest weight of 0.200 is found for wind turbines.

It is confirmed by the decomposition results that the effective dispatch contribution coefficient stems from the joint effect of resource physical attributes and communication conditions, which aligns with the theoretical derivation presented in Section 2.1.

Table 3 presents a comparison of the net revenue of each resource agent under independent operation and VPP coordinated dispatch.

Table 3. Revenue comparison of each resource agent between independent operation and VPP coordinated dispatch.

Resource Agent	Independent Operation (CNY)	After VPP Dispatch (CNY)
Wind turbines	54,248	55,213
Photovoltaic units	15,967	16,372
Energy storage batteries	10,717	11,087
Electric vehicles	10,331	10,858
Air-conditioning loads	−36,985	−35,217

Following integration into the VPP aggregation framework, revenue growth or loss mitigation is achieved across all resource agents. Specifically, revenue increases of 1.78%, 2.54%, 3.45%, and 5.10% are recorded for wind turbines, photovoltaic units, battery energy storage systems, and electric vehicles, respectively, while the operating loss of air-conditioning loads is reduced by 4.78%. Such performance improvements are attributed to the complementary characteristics of heterogeneous resources. Temporal power transfer is realized by the VPP via energy storage systems and electric vehicles, and the peak–valley load difference is mitigated through air-conditioning demand response, thereby enhancing the overall operational economy.

Figure 5 further illustrates the proportional contribution of each resource agent to the total VPP revenue increment.

https://doi.org/10.3390/wevj17090484

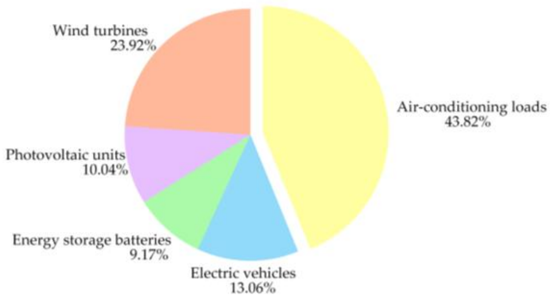

Figure 5. Contribution of each resource agent to total revenue improvement after VPP dispatch.

The largest contribution share of 43.82% is attributed to air-conditioning loads, as their operating losses are substantially reduced through coordinated peak shaving. Wind turbines and electric vehicles account for 23.92% and 13.06%, respectively, with the gains primarily derived from reduced renewable curtailment and optimized charge–discharge arbitrage. Photovoltaic units and battery energy storage systems contribute 10.04% and 9.17% of the total improvement, respectively. This contribution distribution indicates that demand-side flexible loads serve as the primary source of revenue enhancement in VPP aggregated dispatch.

A total net revenue of CNY 58,313 is attained by the VPP under the proposed method, representing a 7.43% increase compared with the CNY 54,278 achieved under independent operation. These findings corroborate the economic viability of VPP aggregated dispatch. Coordinated optimization elevates the utilization efficiency of flexible resources and lowers the overall operating cost of the system.

Table 4 summarizes the net revenue of each individual resource agent as well as the aggregate VPP revenue across the three scenarios.

Table 4. Net revenue comparison under three scheduling scenarios.

Resource Agent	Scenario 1	Scenario 2	Scenario 3 (CNY)
Wind turbines	55,213	54,725	54,982
Photovoltaic units	16,372	15,998	16,195
Energy storage batteries	11,087	10,624	10,873
Electric vehicles	10,858	10,117	10,536
Air-conditioning loads	−35,217	−35,792	−35,516
Total	58,313	55,672	57,070

The highest total net revenue of CNY 58,313 is recorded under Scenario 1, followed sequentially by Scenario 3 and Scenario 2.

Compared with Scenario 2, in which scheduling uncertainty is entirely disregarded, a 4.74% increase in total revenue is achieved under Scenario 1. Among all resource categories, the most substantial loss reduction is observed for air-conditioning loads, while the highest revenue growth rate is attained by electric vehicles, at 1.61% and 7.32%, respectively. This performance gap is attributed to their relatively high effective dispatch contribution coefficients, which enable these resources to undertake more dispatch tasks and accrue greater revenue.

Relative to Scenario 3, where only the communication failure probability is incorporated into the execution-reliability quantification, a revenue improvement of 2.18% is still achieved under Scenario 1. To separate the benefit of reliability modeling from that of overall coordination, an additive ablation is performed along the nested scenarios. Scenario 2 is the baseline; adding only communication execution reliability, so that the share weight degenerates to $\beta_i = P_{s,i}$, gives Scenario 3; further adding the relative capacity weight,

$\beta_i = w_i P_{s,i}$, gives Scenario 1, so that each step isolates a single mechanism. Adding communication execution reliability alone raises total net revenue by CNY 1398 (+2.51%), and adding the relative capacity weight on top of it raises it by a further CNY 1243 (+2.18%). The two contributions are of comparable magnitude, accounting for 53% and 47% of the combined CNY 2641 (+4.74%) gain, which shows that the advantage is neither a single-mechanism artefact nor a generic coordination benefit, but is attributable in near-equal measure to modeling execution reliability and to reliability-aware weighting; the same ordering holds for every resource (for the EV fleet the two steps contribute CNY 419 and CNY 322, totaling the reported +7.32%).

The two EV compliance rates are separated in the same closed-form manner through $P_{s,\mathrm{EV}} = P_{s,\mathrm{base}}[m\ r_{\mathrm{oc}} + (1 - m)\ r_{\mathrm{V2G}}]$. Collapsing them to a single common rate would bias the EV composite reliability: setting both to the orderly rate 0.95 overstates it to 0.845 (+9.2%), whereas setting both to the V2G rate 0.75 understates it to 0.667 (−13.8%), bracketing the differentiated value 0.774; the unit marginals are 0.534 for r_{oc} and 0.356 for r_{V2G}. Distinguishing charging from V2G compliance therefore removes a systematic over-estimation/under-estimation rather than adding redundant detail.

Figure 6 decomposes the aggregate VPP revenue into four constituent components: total transaction revenue, total compensation benefit, total dispatch cost, and total aggregation cost.

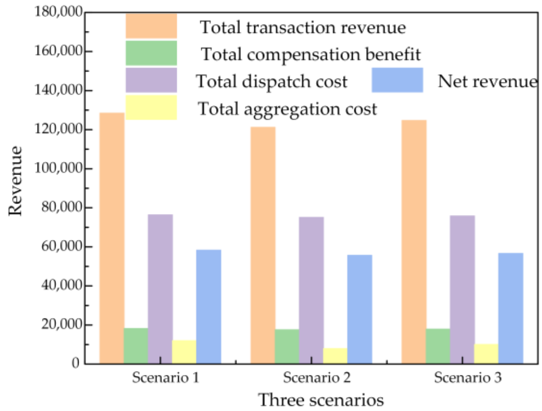

Figure 6. Revenue composition comparison under three scheduling scenarios.

The revenue disparity across scenarios is primarily driven by two factors on the income side: higher transaction revenue and compensation benefits are attained under Scenario 1 via enhanced renewable energy accommodation. On the cost side, correspondingly elevated aggregation costs are incurred, as communication management and capacity weight evaluation are explicitly incorporated into the scheduling framework.

Overall, the revenue increment delivered by precise scheduling decisions substantially exceeds the additional aggregation costs incurred. Because Table 4 reports net revenue after all dispatch and aggregation costs, including communication management and capacity-weight evaluation, the CNY 264 advantage of Scenario 1 over Scenario 2 is already net of the added communication and aggregation expenditure: the proposed scheme breaks even only if that extra expenditure were to rise by a further CNY 2641, i.e., by the entire net gain. Under the less favorable parameters tested in Section 4.3 (a doubled V2G degradation cost and compliance rates perturbed by ±0.05), the revenue ordering S1 > S3 > S2 is unchanged, so the additional aggregation and communication cost remains economical.

Figures 7–9 present the 24 h capacity-layer allocation profiles—the per-period regulation capacity assigned to each of the five resource categories—under Scenarios 1–3. For the EV fleet, the actual charge/discharge power is forced to zero during the off-grid interval [7,19] by Equation (30), even though a non-zero capacity-layer allocation may remain in Figures 7–9; any EV capacity allocated but not deliverable over that interval is re-dispatched through the recourse procedure described in Section 4.4.

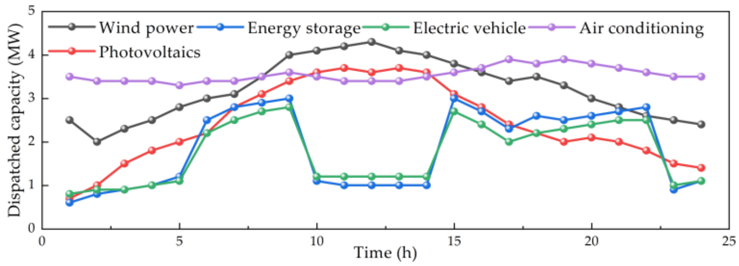

Figure 7. Capacity-layer dispatched capacity of each resource agent under Scenario 1.

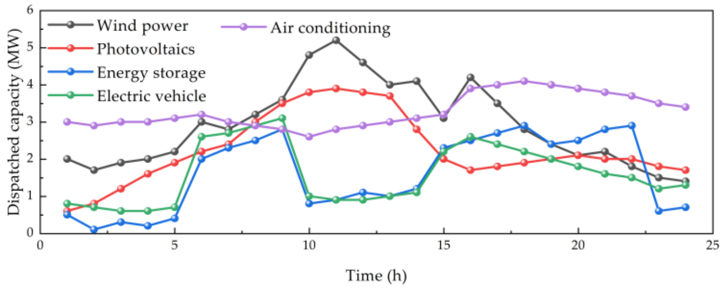

Figure 8. Capacity-layer dispatched capacity of each resource agent under Scenario 2.

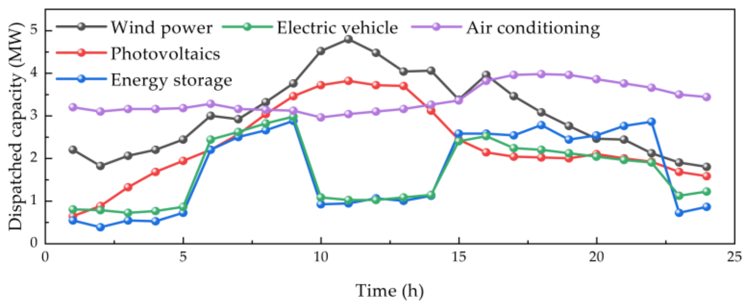

Figure 9. Capacity-layer dispatched capacity of each resource agent under Scenario 3.

The allocated capacity of storage and EV is concentrated within the EV grid-connected windows: it is directed to surplus absorption during 00:00–07:00 and to peak support during 19:00–22:00, whereas no EV power is physically executed over the off-grid interval [7,19].

When compared across the three scenarios, the most severe fluctuation in dispatched capacity is observed in Scenario 2, with charge–discharge behavior highly concentrated during peak and valley periods. By contrast, a far smoother dispatch profile is achieved under Scenario 1. During the representative evening peak interval (19:00–22:00), the total discharge power of energy storage systems and electric vehicles under Scenario 1 is 12.7% lower than that under Scenario 2, with a more uniform output distribution.

The underlying mechanism for this difference is that dispatch tasks are allocated by the proposed method in accordance with the effective dispatch contribution coefficient, which prevents excessive concentration of dispatch instructions on low-reliability resources. This design mitigates the risk of dispatch failure and flattens the net load profile. Correspondingly, the peak–valley difference in the net load under Scenario 1 is reduced by 8.3% relative to Scenario 2. The dispatched capacity under Scenario 3 falls between the values of the two aforementioned scenarios, which further corroborates that partial consideration of uncertainty delivers only limited optimization of the scheduling scheme.

Figure 10 depicts the hourly actual accommodated renewable power under the three scenarios.

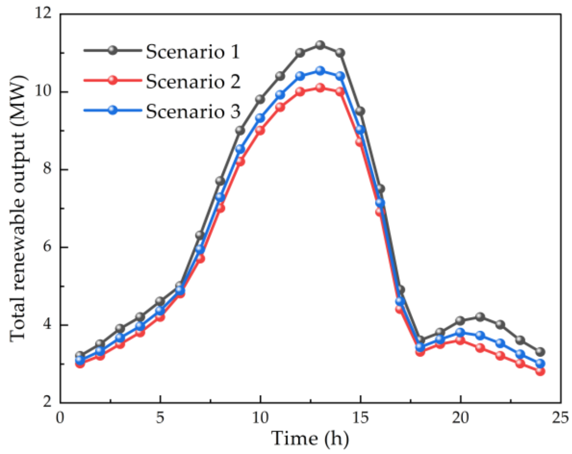

Figure 10. Comparison of accommodated renewable power under three scenarios.

On the whole, the accommodated renewable power under Scenario 1 remains consistently higher than that under Scenario 2 and Scenario 3 throughout the entire scheduling horizon, with the most notable gap emerging during the midday photovoltaic output peak (11:00–15:00).

Quantitatively, the maximum accommodation gap between Scenario 1 and Scenario 2 is observed at 12:00, reaching 1.0 MW, which coincides with the period of peak photovoltaic output. During this interval, surplus photovoltaic power is absorbed more proactively by the energy storage system under Scenario 1, effectively mitigating photovoltaic curtailment. During the nighttime wind power period (00:00–06:00), the accommodation gap remains relatively narrow, yet an advantage of approximately 0.4–0.6 MW is still maintained by Scenario 1.

This phenomenon can be attributed to the scheduling execution rate. Accurate evaluation of the effective dispatch contribution coefficient eliminates the mismatch between scheduled capacity and actual response capability, thereby enhancing the practical utilization efficiency of renewable energy.

Table 5 summarizes the key indicators of renewable energy accommodation and operational economy across the three scenarios.

Table 5. Renewable energy accommodation rate and average operating cost under three scenarios.

Indicator	Scenario 1	Scenario 2	Scenario 3
Renewable energy accommodation rate (%)	94.6	88.3	91.5
Average operating cost (CNY/MWh)	312	331	321

A renewable energy accommodation rate of 94.6% is attained under Scenario 1, representing an increase of 6.3 percentage points relative to Scenario 2 and 3.1 percentage points relative to Scenario 3. Meanwhile, the average operating cost is reduced from 331 CNY/MWh under Scenario 2 to 312 CNY/MWh under Scenario 1, corresponding to a reduction ratio of 5.74%. The simultaneous improvement in both accommodation performance and economic efficiency corroborates that the proposed scheduling strategy achieves a win-win outcome in terms of clean energy consumption and cost reduction.

Figures 11–13 illustrate the overall optimal dispatch results of the VPP across the three scenarios, in which positive values denote power injection and negative values denote power absorption.

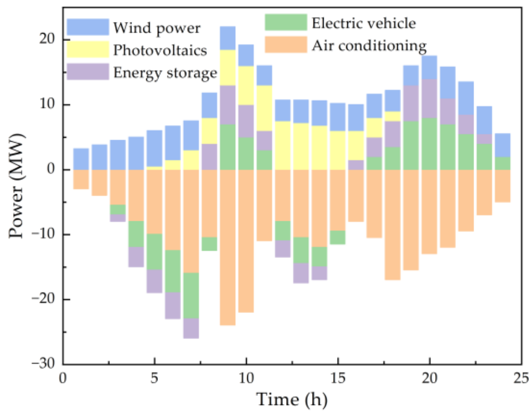

Figure 11. Optimal VPP dispatch result under Scenario 1.

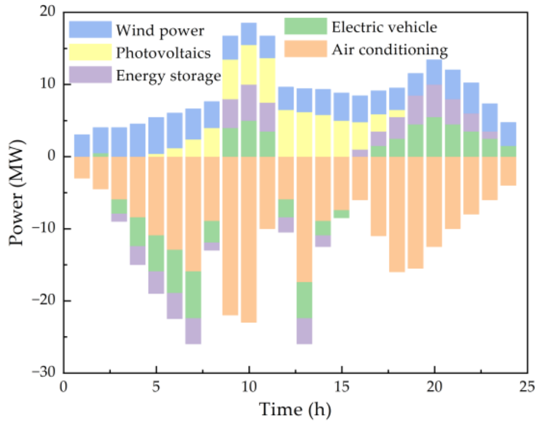

Figure 12. Optimal VPP dispatch result under Scenario 2.

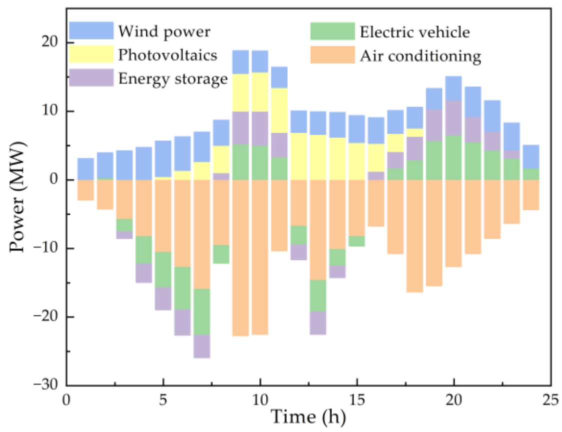

Figure 13. Optimal VPP dispatch result under Scenario 3.

The dispatch schemes across all three scenarios follow the canonical peak-shaving and valley-filling pattern, and are divided into four operational stages according to source-load characteristics:

Low-load period (00:00–06:00): Wind power output remains relatively low and primarily serves the base air-conditioning load. Electricity is purchased by the VPP from the utility grid to charge energy storage systems and electric vehicles, storing energy for the subsequent peak load period.

Load ramp-up period (07:00–11:00): Renewable generation is insufficient to satisfy the growing load demand. Energy storage systems are switched to discharging mode to supplement power supply and lower electricity procurement costs. Electric vehicles are off-grid during this period and do not participate in dispatch.

Renewable generation peak period (12:00–16:00): Photovoltaic output reaches its daily maximum, and total renewable generation exceeds the load demand. Surplus electricity is absorbed by energy storage systems operating in charging mode, thereby avoiding renewable curtailment. Electric vehicles remain off-grid during this period.

Evening peak period (17:00–23:00): Photovoltaic output declines progressively while the load rises to its evening peak. Energy storage systems are discharged to provide peak shaving support from 17:00, and electric vehicles join the discharge upon grid connection at 19:00, collectively providing peak shaving support through 23:00.

In comparison, a larger charge–discharge amplitude and more severe power fluctuation are observed in Scenario 2, whereas milder fluctuation and more reasonable power distribution are achieved under Scenario 1. This discrepancy essentially arises from the fact that the response risk of each resource is quantified in Scenario 1 and aggressive dispatch schemes are avoided, yielding a more robust scheduling outcome.

Figures 14 and 15 further compare the wind power and photovoltaic accommodation curves across the three scenarios, respectively.

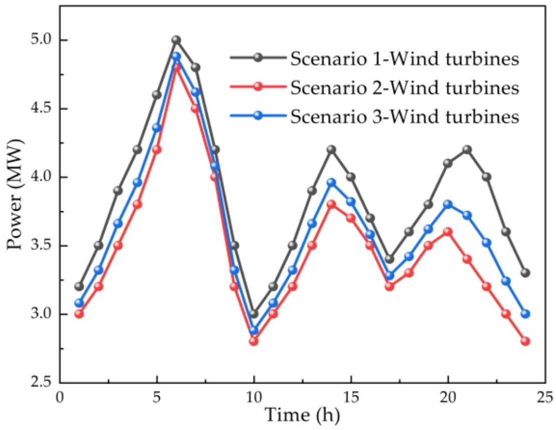

Figure 14. Comparison of wind power accommodation under three scenarios.

For wind power, the accommodation gap across scenarios remains relatively stable throughout the day. The highest accommodation level is sustained under Scenario 1, with an average accommodated power of 3.96 MW, followed by Scenario 3 at 3.77 MW and Scenario 2 at 3.63 MW. This stable gap indicates that the scheduling success probability exerts a persistent influence on wind power consumption.

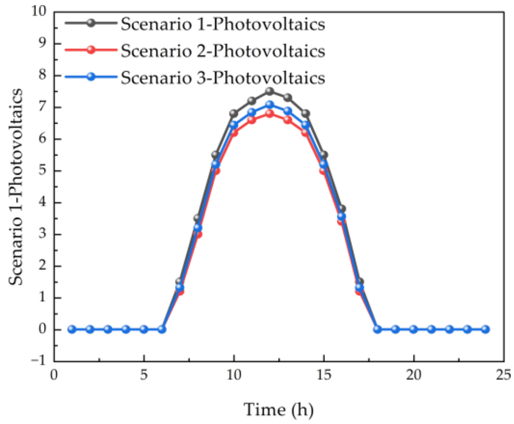

Figure 15. Comparison of photovoltaic accommodation under three scenarios.

For photovoltaic generation, the accommodation gap exhibits a pronounced inverted V-shaped distribution: it widens with the rise of photovoltaic output and narrows as output declines. The maximum gap occurs at 12:00, which aligns closely with the peak photovoltaic output. This pattern suggests that the advantage of the proposed method becomes more prominent under high renewable output conditions, as flexible resources can be mobilized more effectively to absorb surplus power.

Overall, energy storage systems and electric vehicles fulfill the function of temporal energy shifting across all scenarios. Nevertheless, a higher renewable accommodation level and more rational output distribution are achieved under Scenario 1, which corroborates the effectiveness of the proposed scheduling strategy.

4.3. Robustness Verification and Algorithm Convergence Analysis

To verify the robustness of the proposed method under varying parameter settings, single-factor sensitivity analysis is performed with respect to three key parameters: communication channel capacity, dispatch price upper bound, and agent scale.

Figure 16 depicts the variations in the average effective dispatch contribution coefficient and total VPP revenue as a function of the channel capacity scaling factor.

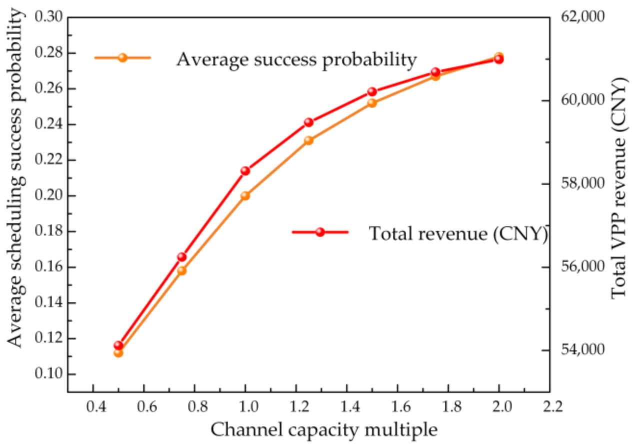

Figure 16. Influence of channel capacity on average effective dispatch contribution coefficient and total VPP revenue.

Overall, both indicators follow a monotonically increasing trend with the escalation of channel capacity, whereas the growth rate tapers off progressively, exhibiting a distinct marginal diminishing effect.

Specifically, when the channel capacity scaling factor is below 1.2, the total revenue rises sharply from CNY 54,120 to CNY 59,478, corresponding to a growth rate of 9.9%. Within this interval, communication delay serves as the primary bottleneck constraining scheduling performance, and the dispatch response failure probability can be substantially reduced by upgrading channel conditions. When the channel capacity scaling factor exceeds 1.5, revenue growth decelerates markedly: an increase from 1.5 to 2.0 yields a revenue increment of merely CNY 777, representing a growth rate of 1.29%. At this stage, communication delay has been reduced to a low level, and the effective dispatch contribution coefficient is predominantly constrained by the relative capacity weight, resulting in a notable decline in the marginal benefit of further communication condition improvements.

This variation pattern aligns with the Shannon–Hartley theorem and the underlying mechanism of the proposed probability model, which corroborates the model's rationality from the perspective of sensitivity analysis.

Figure 17 illustrates the variation profiles of VPP net revenue and renewable energy accommodation rate with respect to the upper bound of the internal dispatch price.

In line with the theoretical derivation presented in Section 3, the net revenue of the VPP exhibits a monotonically increasing trend with the price ceiling, as the optimal dispatch price invariably settles at the upper bound of the feasible interval under positive marginal revenue.

However, a divergent trend is observed for the renewable energy accommodation rate. When the price ceiling is below 500 CNY/MWh, the accommodation rate rises rapidly from 87.2% to 94.6%, corresponding to a growth rate of 8.49%. In this phase, additional schedulable capacity of flexible resources can be continuously mobilized via price elevation to absorb renewable energy. When the price ceiling exceeds 600 CNY/MWh, the accommodation rate gradually stabilizes at approximately 95%, and further price increments exert a negligible effect on accommodation improvement. This is attributed to the fact that the schedulable capacity of each resource agent has reached its physical upper limit, such that higher prices fail to stimulate additional response capacity.

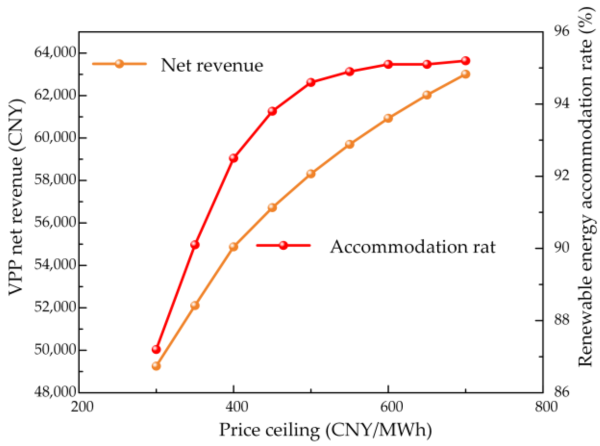

Figure 17. Influence of dispatch price ceiling on net revenue and renewable accommodation rate.

This finding indicates that an optimal balance interval exists between economic benefits and renewable accommodation performance in price parameter configuration. Within the range of 500–600 CNY/MWh, both economic and environmental benefits can be effectively coordinated.

Figure 18 depicts the variations in solution time and iteration count with respect to the scale of resource agents.

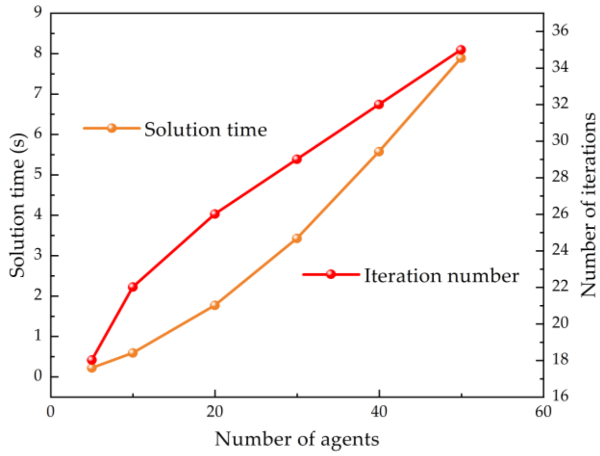

Figure 18. Influence of agent number on solution time and iteration times.

Numerical results indicate that the solution time exhibits an approximately linear growth with the number of agents, while the number of iterations rises at a moderate pace.

Specifically, as the number of agents increases from 5 to 50, the solution time for the 24 h scheduling horizon grows from 0.21 s to 7.89 s, remaining within 8 s, whereas the number of iterations merely increases from 18 to 35. The near-linear growth of computational cost is attributed to the analytical optimal response formulation of each agent under the backward induction framework, which circumvents the curse of dimensionality induced by centralized optimization.

This finding confirms that the proposed algorithm features favorable computational scalability. It can sustain high solution efficiency even for medium-scale VPP systems, thus satisfying the real-time requirements of practical engineering applications.

Figure 19 illustrates the convergence process with dual vertical axes, where the left axis corresponds to the VPP net revenue and the right axis corresponds to the maximum capacity deviation across all agents.

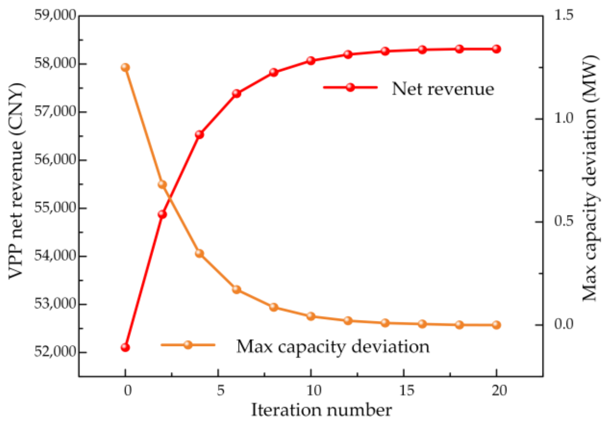

Figure 19. Convergence curve of the backward induction algorithm.

It can be observed from the figure that the VPP net revenue rises monotonically as the iteration count increases, whereas the maximum capacity deviation declines continuously throughout a smooth, oscillation-free convergence process.

Quantitatively, the algorithm attains engineering convergence after 18 iterations, with the net revenue stabilizing at approximately CNY 58,313 and a relative error below 0.01%. Upon reaching 20 iterations, the maximum capacity deviation falls to the magnitude of 10^{-4} MW, which fully satisfies the precision criteria for power system scheduling. The monotonic convergence observed in the case study is consistent with the concavity of each individual agent's objective function and the strict concavity of the Stage 1 VPP revenue function, indicating that the algorithm can provide reliable scheduling solutions for the VPP system studied in this paper under the given parameter settings.

To further verify that the coupled Nash–Stackelberg equilibrium reached in the case study is unique and stable, the best-response procedure was re-launched from five markedly different initial capacity profiles.

As shown in Figure 20a, every start converges to the identical equilibrium revenue of CNY 58,313, with a relative gap below 0.01% after 18 iterations; the corresponding maximum cross-agent capacity mismatch in Figure 20b decays smoothly and without oscillation to the 10^{-4} MW tolerance within 20 iterations. Together with the strict concavity of every follower objective and the strict concavity of the Stage 1 objective, this multi-start consistency provides numerical evidence that the equilibrium of the studied system is unique and stable.

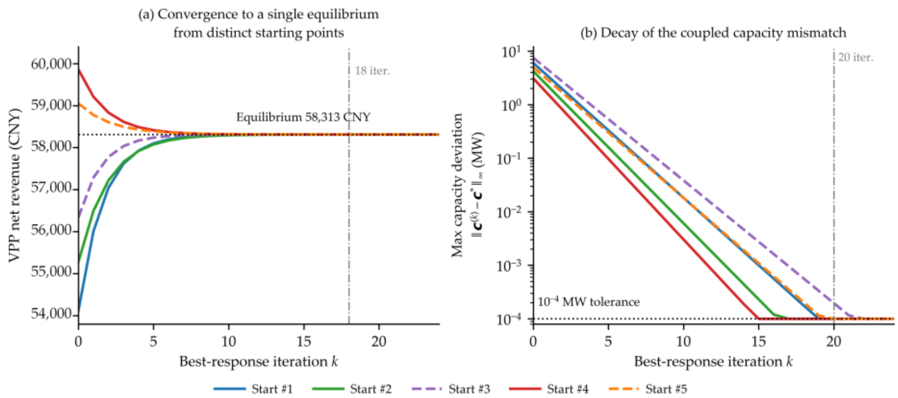

Figure 20. Multi-start verification of the coupled Nash–Stackelberg equilibrium.

Figure 21 examines the analytical behavior of the execution-reliability model.

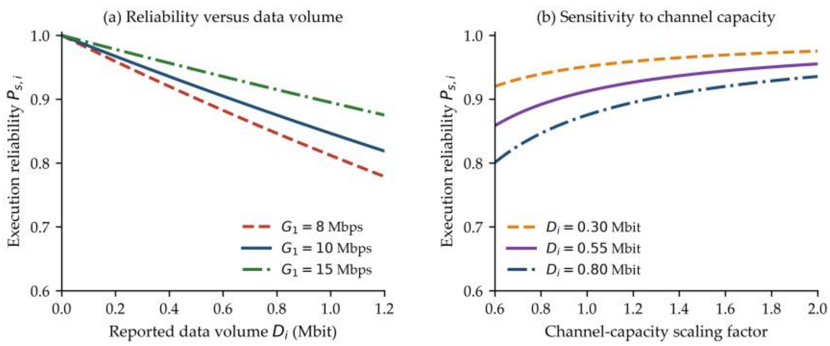

Figure 21. Analytical behavior of the execution-reliability model.

As shown in Figure 21a, the execution reliability decreases monotonically with the reported data volume D_i, while a larger channel capacity G_1 shifts the entire curve upward; under the baseline G_1 = 10 Mbps, G_2 = 1.2, and T = 0.5, it remains above 0.88 over the payload range of the five agents. Figure 21b shows that it rises with the channel-capacity scaling factor with a diminishing marginal gain, which is consistent with, and supplies the probabilistic basis for, the revenue trend in Figure 16. These results confirm that Equation (7) is well behaved over the entire parameter range of the case study and that the conclusions are not tied to a particular choice of communication parameters.

Figure 22 maps in closed-form the electric vehicle composite reliability defined by the corresponding governing equations across a joint, empirically plausible compliance domain.

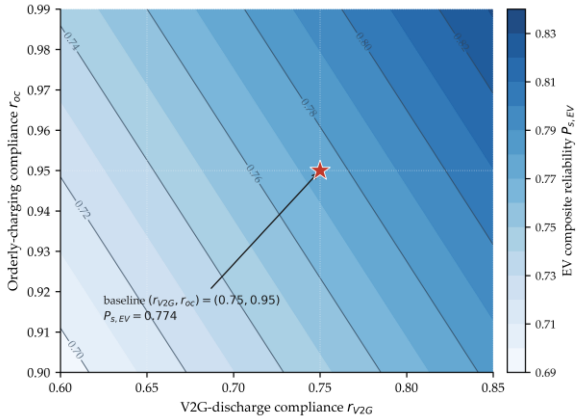

Figure 22. EV composite execution reliability response surface over the joint compliance domain.

As the underlying expression constitutes a linear mixture, the resulting response surface forms a plane featuring parallel, equally spaced contours. The composite reliability remains confined within a fixed interval, varies monotonically with both compliance coefficients, and exhibits no interior extremum or abrupt variation, while the baseline operating point sits close to the domain center. This bounded, smooth behavior demonstrates that the observed electric vehicle revenue improvement is robust to realistic uncertainty in estimated compliance rates, instead of being dependent on specific point estimates. Quantitatively, perturbing both compliance rates simultaneously by ±0.05—a band wider than the statistical confidence interval of the estimates—moves the EV composite reliability only within [0.730, 0.819] about the baseline 0.774, leaving its sign, ordering, and the interior equilibrium unchanged.

To further validate the EV-specific contribution, closed-form sensitivity analyses are performed for the six EV parameters, separated according to the model layer at which each acts, as shown in Figure 23.

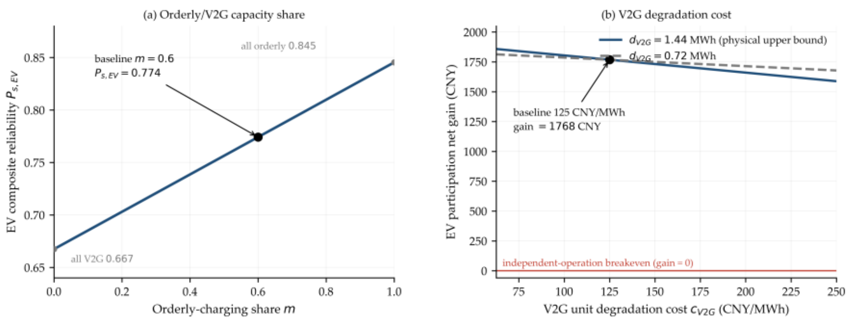

Figure 23. Closed-form strategic-layer sensitivity of the EV agent.

At the strategic/probability layer, the orderly/V2G share affects composite reliability linearly: as it runs from all-V2G to all-orderly, the EV self-provision probability spans [0.667, 0.845] and passes through the baseline 0.774, remaining bounded and positive throughout. The V2G unit degradation cost does not alter declared capacity at this layer; it only shifts net revenue and the individual-rationality threshold. Even when this cost is varied from half to double its baseline, and the V2G dispatch is conservatively set to its physical upper bound, the EV participation net gain over independent operation falls by at most 24.5% and stays strictly positive, so EV participation is robust to degradation-cost uncertainty.

At the physical layer, because the fleet may repeatedly charge and discharge within its grid-connected window, its maximum daily V2G energy is a deterministic envelope obtained directly from the energy balance and the cycle-life limit, with no re-optimization, as shown in Figure 24.

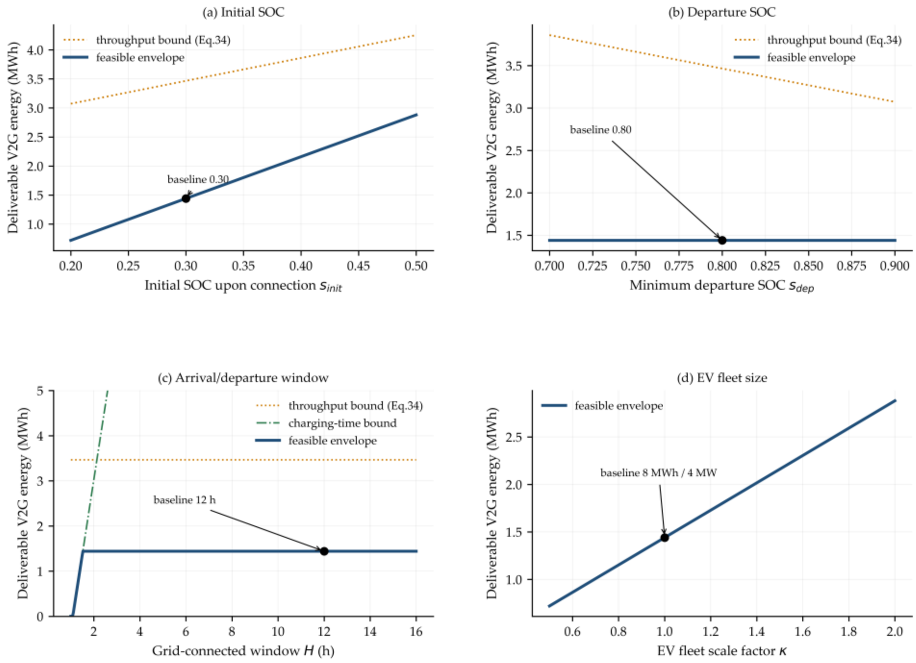

Figure 24. Maximum daily deliverable V2G energy envelope.

At the baseline setting (initial SOC 0.30, departure SOC 0.80, 12 h window, 8 MWh/4 MW fleet), the fleet can deliver at most 3.47 MWh of V2G energy, for which the active bound is the daily cycle-throughput limit, whereas the charge/discharge time and SOC-range limits remain slack. Raising the initial SOC from 0.20 to 0.50 enlarges the envelope from 3.07 to 4.25 MWh; raising the required departure SOC from 0.70 to 0.90 reduces it mildly from 3.86 to 3.07 MWh; and the envelope saturates once the window exceeds only about 2.1 h, so the reported 19:00–07:00 window—and indeed any 8–16 h window—lies well inside the flat region. Scaling the fleet rescales the envelope linearly. Across all reported neighborhoods, the physical envelope therefore remains ample and never binds the strategic interior optimum, confirming that the differentiated EV scheduling result and the riskier-but-profitable V2G statement do not hinge on the single chosen fleet, SOC, or window setting.

4.4. Monte Carlo Robustness Verification Under Stochastic Scenarios

To verify the actual operational performance of the proposed scheduling strategy when facing stochastic dispatch execution failures, a large number of random scenario simulations are carried out based on the Monte Carlo method, and the statistical characteristics and risk levels of key operation indicators are quantitatively evaluated.

The selected representative day spans all three canonical net-load regimes: night-time wind surplus with charging (00:00–07:00), the midday photovoltaic peak (11:00–14:00), and the evening load peak with V2G discharge (19:00–22:00), while the five agents cover the four functional types of generation, storage, mobile storage (EV), and controllable load. Its representativeness is supported in two further ways. First, the equilibrium admits the closed forms of Equations (49) and (55), so the interior optimum and the revenue ordering are structural results that hold for any profile within the analyzed parameter bands rather than for one specific trajectory; the dedicated sensitivity analyses on channel capacity (Figure 16), price ceiling (Figure 17), agent number (Figure 18), EV compliance (Figure 22), and the six EV physical/strategic parameters (Figures 23–24) already sweep the corresponding parameter space. Second, source/load forecast error, distribution-network congestion, and price uncertainty are uncertainty sources orthogonal to the communication execution failure studied here and are addressed by established stochastic, robust, or chance-constrained formulations [33–35] that can be combined with the proposed reliability term; consistent with the scope stated in Section 2, transient network constraints are handled by the lower multi-period layer, and their explicit co-optimization is left to future work. The Monte Carlo study below therefore targets the execution-failure dimension specific to this paper.

By this rule, the Monte Carlo trial reproduces the agent-specific reliability of Equation (7) rather than a data-independent constant. Figure 25 confirms the agreement: over 1000 trials, the empirical success frequency of every agent lies on the 45° line within its 95% binomial confidence band. This is a model-consistent robustness check, not an independent empirical test of the Poisson assumption. The specific simulation process is as follows:

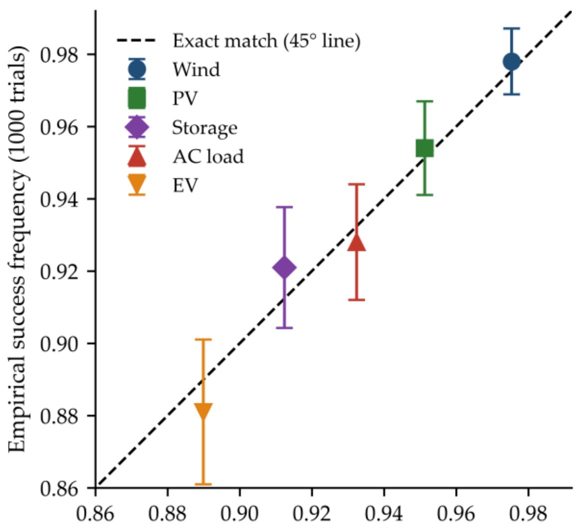

Figure 25. Consistency between the Monte Carlo trial and the analytical model.

Take the optimal dispatch scheme obtained by deterministic optimization as the baseline plan, including the scheduled capacity of each resource agent in each time period.

For each agent in each period, draw the effective service margin X~Exp(T) and declare success if and only if $X \geq \Delta t_i = \dfrac{D_i}{G_1 G_2}$; otherwise, the agent's schedulable capacity cannot be executed. By construction, the failure probability is exactly $1-P_{s,i}$ in Equation (2).

Post-failure re-dispatch. When an agent fails, a cost-ordered recourse preserves the power balance of Equation (21): the imbalance is first re-allocated among the online flexible agents in proportion to their η_i, then covered by upstream-grid reserve; renewable curtailment and relaxation of the controllable-load comfort band are used only as last resorts, and any mismatch still remaining is recorded as power imbalance, whose relative frequency is the reserve shortage probability. The SOC and indoor-temperature states are then re-propagated from the re-dispatched power. Hence, the 0.32 MW average imbalance, 1.12% violation time ratio, and 1.20% reserve shortage probability in Table 6 are residual post-recourse quantities, confirming that the schedule together with this recourse chain closely tracks feasible VPP operation under random execution failures.

Calculate the actual operation state of the system based on the actual response capacity, including power balance, renewable energy curtailment, energy storage SOC, indoor temperature, and net revenue.

Repeat the above random sampling and operation calculation 1000 times to obtain the sample set of operation indicators, and count the distribution characteristics, confidence intervals, and risk indicators. Following standard practice in power system Monte Carlo analysis, 1000 independent trials are conducted to ensure stable estimation of the mean and dispersion of key operation indicators.

Two scheduling schemes are compared in the test: the proposed method (Scenario 1) and the conventional method without considering execution reliability (Scenario 2), to highlight the robustness advantage of the proposed method in stochastic scenarios.

Table 6 summarizes the statistical characteristics of core operation indicators under 1000 Monte Carlo simulations, including mean value, standard deviation (SD), and 95% prediction interval (PI), where the PI is defined as mean ± 1.96·SD and covers approximately 95% of the simulated outcomes.

Table 6. Statistical characteristics of core operation indicators under Monte Carlo simulation.

Indicator	Scenario 1 (Proposed)			Scenario 2 (Conventional)		
	Mean	Std. dev.	95% PI	Mean	Std. dev.	95% PI
VPP net revenue (CNY)	58,127	512	[57,124, 59,130]	55,219	894	[53,466, 56,972]
Average power imbalance (MW)	0.32	0.11	[0.10, 0.54]	0.59	0.23	[0.14, 1.04]
Renewable curtailment (MWh)	7.82	1.25	[5.37, 10.27]	14.26	2.74	[8.89, 19.63]
Dispatch failure capacity ratio (%)	3.18	0.87	[1.47, 4.89]	7.45	1.62	[4.27, 10.63]
Constraint violation time ratio (%)	1.12	0.56	[0.02, 2.22]	2.68	1.03	[0.66, 4.70]
Reserve shortage probability (%)	1.20			5.80		

Note: The 95% prediction interval (PI) for continuous indicators is defined as mean ± 1.96·SD. The reserve shortage probability is the relative frequency across 1000 trials, with 95% confidence intervals of [0.53%, 1.87%] for Scenario 1 and [4.35%, 7.25%] for Scenario 2.

The statistical results show that the mean value of VPP net revenue under Monte Carlo simulation is highly consistent with the deterministic optimization result, which verifies the accuracy of the expected value model established in this paper. Compared with the conventional method, the standard deviation of net revenue of the proposed method is reduced by 42.7%, and the width of the 95% prediction interval is narrowed by 42.8%, indicating that the revenue fluctuation is significantly smaller and the operation stability is stronger. The average power imbalance, renewable curtailment, and dispatch failure ratio of the proposed method are all significantly lower than those of the conventional method, which confirms that considering execution reliability in the scheduling stage can effectively reduce the deviation between actual operation and planned dispatch and improve the controllability of the operation state. The constraint violation ratio and reserve shortage probability are maintained at a low level under the proposed method, which means that the scheduling scheme has stronger adaptability to random execution failures and can better guarantee the safe operation of the system.

Because the EV is the only agent subject to both communication failure and user non-compliance, their simultaneous occurrence is examined in closed form through the product $P_{s,\mathrm{EV}} = P_{s,\mathrm{base}}[\mathrm{m}\ r_{\mathrm{oc}} + (1 - \mathrm{m})\ r_{\mathrm{V2G}}]$. Taking halved channel capacity ($P_{s,\mathrm{base}}$ falling from 0.890 to 0.792) as the communication stress and a 0.05 reduction in both compliance rates as the behavioral stress, the single stresses lower $P_{s,\mathrm{EV}}$ from 0.774 to 0.689 and 0.730, respectively, whereas their joint occurrence lowers it to 0.649; even under the extreme combination of quarter channel capacity and a 0.10 compliance drop, it remains 0.483. Because the two factors enter multiplicatively, the joint effect is bounded by their product and exhibits no catastrophic interaction: $P_{s,\mathrm{EV}}$ stays positive, and the interior equilibrium together with the revenue ordering S1 > S3 > S2 is unchanged, confirming robustness to simultaneous communication and compliance failures without an additional simulation run.

4.5. Comparison with Established Scheduling Approaches

To position the proposed framework relative to established paradigms rather than only the internal ablation scenarios, Table 7 compares it with three representative VPP/EV scheduling methods: two-stage distributionally robust optimization with EV virtual energy storage [33], a CVaR-based VPP–EV Stackelberg game [34], and information-gap decision theory (IGDT) bi-layer EV scheduling [35].

Table 7. Structural comparison of the proposed framework with established VPP/EV scheduling approaches.

Aspect	DRO + EV−VES [33]	CVaR Stackelberg [34]	IGDT bi-Layer [35]	Proposed
Uncertainty modeled	source/load forecast error, Wasserstein ambiguity set	EV charge–discharge behavior, CVaR tail risk	renewable output, info-gap interval	communication-induced execution failure, Poisson/exp
EV/V2G treatment	EV as virtual energy storage	differentiated charge/discharge under CVaR	spatial-temporal EV dispatch	orderly vs. V2G differentiated by compliance
Decision structure	single-operator two-stage, C&CG	VPP–EV Stackelberg, PSO iteration	bi-layer cost minimization	two-stage Stackelberg, closed-form best response
Per-agent execution reliability	No	No	No	Yes, explicit $P_{s,i}$
Closed-form equilibrium	numerical C&CG	numerical PSO	numerical bi-level	yes, Equations (49) and (55)
Post-failure recourse	No	No	No	yes, re-dispatch chain + MC consistency

These established methods are effective for hedging source-load forecast error, EV behavioral risk, and renewable-output interval uncertainty, respectively, but they all implicitly assume that, once a schedule is issued, every resource executes it perfectly; none carries a per-agent probability that declared capacity fails to be delivered because of communication constraints, and none provides a post-failure recourse. The proposed execution-reliability modeling is therefore orthogonal and complementary to stochastic, robust, or chance-constrained formulations, which could be combined with it in future work. A same-system quantitative anchor is given by the ablation in Table 4: Scenario 2 removes the reliability/weight coupling and thus reproduces exactly the perfect-execution assumption shared by the benchmarks above, whereas the full Scenario 1 raises total revenue by 4.74% over Scenario 2 (and by 2.18% over Scenario 3, which omits only the relative weight), with the Monte Carlo results of Table 6 confirming the gain under random dispatch failure.

Because the methods of ref citation [33–35] are evaluated on different test systems and datasets, a direct cross-system numerical ranking would not be meaningful; accordingly, we restrict our superiority claim to the communication-constrained VPP setting and the specific scenarios examined here, and present the structural comparison as evidence that the reported advantage stems from explicitly accounting for execution reliability rather than from the particular form of the scheduling-success function.

https://doi.org/10.3390/wevj17090484

5. Conclusions

To address scheduling deviations caused by heterogeneous response reliability of generalized demand-side resources in VPPs, this paper proposes a two-stage optimal scheduling framework embedded with the effective dispatch contribution coefficient, which explicitly quantifies the differentiated execution risks between EV orderly charging and V2G modes.

From the modeling perspective, the two-dimensional model coupling relative capacity weight and dispatch execution reliability builds a quantitative bridge between communication uncertainties and economic scheduling decisions. The dual-mode performance coefficient designed for EVs avoids the oversimplification of treating EV fleets as static energy storage units, enabling a more accurate depiction of the practical scheduling execution features of mobile user-side resources.

Methodologically, the leader–follower game scheduling model is decoupled via backward induction, and the analytical optimal dispatch price is rigorously derived via KKT conditions. The computational cost of the solution framework grows approximately linearly with the number of agents, exhibiting near-linear scalability for medium-scale VPPs; extension to large-scale VPPs requires further validation. It provides reliable decision support for day-ahead VPP optimal scheduling under the tested parameter settings.

Case study results demonstrate that compared with the conventional benchmark strategy, the proposed method increases the total VPP net revenue by 7.43%, raises the renewable energy accommodation rate by 6.3 percentage points, and reduces the average operating cost by 5.74%. EVs deliver the highest revenue growth rate of 5.10% among all resource types. Monte Carlo stochastic simulation further confirms that it can effectively suppress operational fluctuations and downside risks under random execution failures, with strong robustness.

For practical engineering deployment, the method requires dedicated power communication infrastructures with stable channel capacity as the basic guarantee for dispatch execution reliability. In the implementation process, attention should also be paid to challenges including user participation willingness guidance, standardized access to heterogeneous resources, and operation data security, to ensure safe and efficient system operation.

Future work will extend the proposed framework to scenarios involving the dynamic evolution of user participation willingness and multi-energy coupling operation, to support efficient VPP operation and vehicle-grid integrated smart energy systems under high renewable penetration.

Author Contributions: Conceptualization, D.W.; methodology, M.D.; software, S.G.; validation, Y.J., X.L., S.C. and Y.H.; formal analysis, S.C. and M.D.; investigation, X.L. and Y.H.; resources, Y.J.; data curation, X.L., S.C. and Y.H.; writing—original draft, S.G. and M.D.; writing—review and editing, D.W.; visualization, S.G.; supervision, D.W.; project administration, Y.J.; funding acquisition, Y.J. All authors have read and agreed to the published version of the manuscript.

Funding: This research was funded by the Science and Technology Project of State Grid Liaoning Electric Power Co., Ltd. grant number 2023YF-127.

Data Availability Statement: The original contributions presented in this study are included in the article. Further inquiries can be directed to the corresponding author.

Conflicts of Interest: Yukun Jin, Xiaopeng Li, Siyuan Cai, and Yipin Han are employees of State Grid Anshan Electric Power Supply Company, State Grid Liaoning Electric Power Co., Ltd. The authors declare that this study received funding from State Grid Liaoning Electric Power Co., Ltd. The funder had the following involvement with the study: study design, provision of engineering

data, and partial execution of the research. The remaining authors declare that the research was conducted in the absence of any commercial or financial relationships that could be construed as a potential conflict of interest.

References

1. Pan, C.Y.; Fan, H.T.; Zhang, R.X.; Sun, J.; Wang, Y.; Sun, Y. An improved multi-timescale coordinated control strategy for an integrated energy system with a hybrid energy storage system. *Appl. Energy* **2023**, *343*, 121137. https://doi.org/10.1016/j.apenergy.2023.121137.
2. Shi, J.Q.; Ma, L.Y.; Li, C.C.; Liu, N.; Zhang, J. A comprehensive review of standards for distributed energy resource grid-integration and microgrid. *Renew. Sustain. Energy Rev.* **2022**, *170*, 112957. https://doi.org/10.1016/j.rser.2022.112957.
3. Fan, H.; Yu, Z.C.; Xia, S.W.; Li, X. Review on coordinated planning of source-network-load-storage for integrated energy systems. *Front. Energy Res.* **2021**, *9*, 641158. https://doi.org//10.3389/fenrg.2021.641158.
4. Alahyari, A.; Ehsan, M.; Mousavizadeh, M.S. A hybrid storage-wind virtual power plant (VPP) participation in the electricity markets: A self-scheduling optimization considering price, renewable generation, and electric vehicles uncertainties. *J. Energy Storage.* **2019**, *25*, 100812. https://doi.org/10.1016/j.est.2019.100812.
5. Tian, L.T.; Cheng, L.; Guo, J.B.; Wang, X.; Yun, Q.; Gao, W. A review on the study of management and interaction mechanism for distributed energy in virtual power plants. *Power Syst. Technol.* **2020**, *44*, 2097–2108. https://doi.org/10.13335/j.1000-3673.pst.2019.2193.
6. Lin, X.H.; Yu, L.; Duan, S.Y.; Liu, Y.; Yuan, L.; Chen, X.; Lian, Y. Hierarchical coordinated optimization control strategy for electricity-to-hydrogen DC microgrid system. *Energy Eng.* **2026**, *123*, 11. https://doi.org/10.32604/ee.2026.072845.
7. Yuan, C.; Liu, C.; Chen, S.J.; Xu, W.; Gou, J.; Xu, K.; Li, Z.; Liu, Y. Second-life battery energy storage system capacity planning and power dispatch via model-free adaptive control-embedded heuristic optimization. *Energy Eng.* **2025**, *122*, 3573–3593. https://doi.org/10.32604/ee.2025.067785.
8. Cao, W.; Wang, S.; Xu, M. Optimal scheduling of virtual power plant based on Latin hypercube sampling and improved CLARA clustering algorithm. *Processes* **2022**, *10*, 2414. https://doi.org/10.3390/pr10112414.
9. Li, B.; Qi, B.; Ali, R.; Siddique, A.; Aslam, W.; Pan, H. Optimized Dual ANN Control Technique for Efficient Energy Management System (EMS) of Microgrid. *Energy Sci. Eng.* **2026**, *14*, 2070–2092. https://doi.org/10.1002/ese3.70465.
10. Aslam, W.; Bhatti, M.Z.A.; Siddique, A.; Atiq, S.; Khan, M.S.; Qamar, H.G.M.; Momal, B.; Abdelwahab, S.A.M.; Agajie, T.F.; Hamada, A.M.; et al. Design and performance evaluation of an islanded hybrid microgrid for an industrial warehouse. *Results Eng.* **2025**, *28*, 107494. https://doi.org/10.1016/j.rineng.2025.107494.
11. Zamani, A.G.; Zakariazadeh, A.; Jadid, S. Day-ahead resource scheduling of a renewable energy based virtual power plant. *Appl. Energy* **2016**, *169*, 324–340. https://doi.org/10.1016/j.apenergy.2016.02.011.
12. Liu, Y.Y.; Li, M.; Lian, H.B.; Tang, X.; Liu, C.; Jiang, C. Optimal dispatch of virtual power plant using interval and deterministic combined optimization. *Int. J. Electr. Power Energy Syst.* **2018**, *102*, 235–244. https://doi.org/10.1016/j.ijepes.2018.04.011.
13. Riveros, J.Z.; Bruninx, K.; Poncelet, K.; D'haeseleer, W. Bidding strategies for virtual power plants considering CHPs and intermittent renewables. *Energy Convers. Manag.* **2015**, *103*, 408–418. https://doi.org/10.1016/j.enconman.2015.06.075.
14. Xu, B.Q.; Zhao, J.L.; Zhang, P.C.; Fan, S.; He, G.Y. High-proportion renewable energy accommodation method based on customer directrix load and Nash bargaining. *Autom. Electr. Power Syst.* **2023**, *47*, 36–45. https://doi.org/10.7500/AEPS20221130016.
15. Zhou, X.; Han, X.Q.; Li, T.J.; Wei, B.; Li, Y. Master-slave game optimal scheduling strategy for multi-agent integrated energy system based on demand response and power interaction. *Power Syst. Technol.* **2022**, *46*, 3333–3344. https://doi.org/10.13335/j.1000-3673.pst.2022.0399.
16. Pan, H.J.; Gao, H.J.; Liu, C.; Ma, W.; Liu, Y.; Liu, J. Research on coordinated operation optimization strategy of integrated energy service provider and multi-users interest community. *Proc. CSEE* **2021**, *41*, 3195–3206. https://doi.org/10.13334/j.0258-8013.pcsee.200799.
17. Chen, Y.Y.; Shao, J.J.; Chen, J.J.; Chen, X.; Lin, Z.; Wu, Y. Demand response trading model of virtual power plant considering electricity consumption satisfaction degree and response quantity expectation. *Electr. Power Autom. Equip.* **2023**, *43*, 226–234. https://doi.org/10.16081/j.epae.202303005.
18. Gough, M.; Santos, S.F.; Lotfi, M.; Javadi, M.S.; Osorio, G.J.; Ashraf, P.; Castro, R.; Catalao, J.P.S. Operation of a technical virtual power plant considering diverse distributed energy resources. *IEEE Trans. Ind. Appl.* **2022**, *58*, 2547–2558. https://doi.org/10.1109/TIA.2022.3143479.

19. Chen, W.; Qiu, J.; Zhao, J.H.; Chai, Q.; Dong, Z.Y. Bargaining game-based profit allocation of virtual power plant in frequency regulation market considering battery cycle life. *IEEE Trans. Smart Grid* **2021**, *12*, 2913–2928. https://doi.org/10.1109/TSG.2021.3053000.
20. Li, Y.; Chen, Y.X.; He, J.H.; He, G.; Dai, C.; Tong, J.; Lei, W. Optimal dispatch of urban distribution networks considering virtual power plant coordination under extreme scenarios. *Energy Eng.* **2025**, *123*, 9. https://doi.org/10.32604/ee.2025.069257.
21. Qi, H.P.; Sun, W.Y.; Zhao, Y.; Qian, X.; Jiang, X. Optimal operation of virtual power plants based on revenue distribution and risk contribution. *Energy Eng.* **2025**, *123*, 17. https://doi.org/10.32604/ee.2025.069603.
22. Al-Awami, A.T.; Amleh, N.A.; Muqbel, A.M. Optimal demand response bidding and pricing mechanism with fuzzy optimization: Application for a virtual power plant. *IEEE Trans. Ind. Appl.* **2017**, *53*, 5051–5061. https://doi.org/10.1109/TIA.2017.2723338.
23. Yuan, G.L.; Zhong, F.; Zhang, R.; Zhou, T. Combined heat and power scheduling optimization for virtual power plants considering carbon capture and demand response. *Power Syst. Technol.* **2023**, *47*, 4458–4467. https://doi.org/10.13335/j.1000-3673.pst.2022.1786.
24. Zhou, B.; Zhou, J.; Chen, L.L. Optimal scheduling of virtual power plants considering cooling, heating and power under carbon trading mechanism. *Electr. Autom.* **2022**, *44*, 67–70. https://doi.org//10.3969/j.issn.1000-3886.2022.06.021.
25. Yan, Q.Y.; Zhang, M.J.; Lin, H.Y.; Li, W. Two-stage adjustable robust optimal dispatching model for multi-energy virtual power plant considering multiple uncertainties and carbon trading. *J. Clean. Prod.* **2022**, *336*, 130400. https://doi.org/10.1016/j.jclepro.2022.130400.
26. Rahimi, M.; Ardakani, F.J.; Olatujoye, O.; Ardakani, A.J. Two-stage interval scheduling of virtual power plant in day-ahead and real-time markets considering compressed air energy storage wind turbine. *J. Energy Storage* **2022**, *45*, 103599. https://doi.org/10.1016/j.est.2021.103599.
27. Zhu, J.Q.; Duan, P.; Liu, M.B. Electric real-time balance dispatch via bi-level coordination of source-grid-load of power system with risk. *Proc. CSEE* **2015**, *35*, 3239–3247. https://doi.org/10.13334/j.0258-8013.pcsee.2015.13.006.
28. Zhao, F.M.; Fan, Y.F. Bi-level optimal dispatching of multi-energy virtual power plant influenced by TOU price. *Power Syst. Prot. Control* **2019**, *47*, 33–40. https://doi.org/10.19783/j.cnki.pspc.181383.
29. Duan, P.; Zhu, J.Q.; Liu, M.B. Optimal dispatch of virtual power plant based on bi-level fuzzy chance constrained programming. *Trans. China Electrotech. Soc.* **2016**, *31*, 58–67. https://doi.org/10.3969/j.issn.1000-6753.2016.09.008.
30. Starke, A.; Nagaraj, K.; Ruben, C.; Aljohani, N.; Zou, S.; Bretas, A.; McNair, J.; Zare, A. Cross-layered distributed data-driven framework for enhanced smart grid cyber-physical security. *IET Smart Grid* **2022**, *5*, 398–416. https://doi.org/10.1049/stg2.12070.
31. Dong, X.; Wei, X.; Zu, G.; Ma, Y.; Yu, X.; Mu, Y. The charge–discharge compensation pricing strategy of electric vehicle aggregator considering users' response willingness from the perspective of Stackelberg game. *IET Smart Grid* **2024**, *7*, 277–293. https://doi.org/10.1049/stg2.12148.
32. Huang, Z.; Cheng, N.; Jiang, Y. Multi-time-scale scheduling strategy for V2G aggregators considering EV peak-regulating demand response reliability. *High Volt. Eng.* **2025**, *51*, 401–411. https://doi.org/10.13336/j.1003-6520.hve.20231247.
33. Wang, B.; Jiang, Y.; Jiang, M.; Ma, K. Two-stage distributionally robust optimization operation of a virtual power plant considering the virtual energy storage of electric vehicles. *Front. Energy Res.* **2024**, *12*, 1495823. https://doi.org/10.3389/fenrg.2024.1495823.
34. Ma, Q.; Jia, H.; Guo, Y.; Li, P.; Yang, Y.; Liu, D.; Zhao, Z. Stackelberg game optimization strategy of virtual power plants and electric vehicles based on conditional value-at-risk. *Electr. Power Constr.* **2025**, *46*, 53–66. https://doi.org/10.12204/j.issn.1000-7229.2025.07.005.
35. Chen, Y.; Yan, R.; Liang, C.; Zheng, Z.; Zhang, M.; Tang, D. A computation-oriented bi-layer optimization for EV scheduling under renewable uncertainties via information-gap decision theory. *Energies* **2026**, *19*, 3965. https://doi.org/10.3390/en19173965.